

Numerical simulations of ocean surface waves under hurricane conditions: Assessment of existing model performance



Qingxiang Liu^{a,*}, Alexander Babanin^a, Yalin Fan^b, Stefan Zieger^c, Changlong Guan^d, Il-Ju Moon^e

^a Department of Infrastructure Engineering, University of Melbourne, Australia

^b Oceanography Division, Naval Research Laboratory, Stennis Space Center, MS 39529, United States

^c Bureau of Meteorology, Melbourne, Victoria, Australia

^d Physical Oceanography Laboratory, Ocean University of China and Qingdao National Laboratory for Marine Science and Technology, Qingdao, China

^e Typhoon Research Center, Jeju National University, South Korea

ARTICLE INFO

Article history:

Received 16 February 2017

Revised 4 August 2017

Accepted 10 August 2017

Available online 12 August 2017

Keywords:

Spectral wave modelling

WAVEWATCH III

The University of Miami Wave Model

Drag coefficient

Negative wind input

Four-wave nonlinear interaction

ABSTRACT

Using the well-observed hurricane case Ivan (2004) as an example, we investigate and intercompare the performance of two wave models under hurricane conditions. One is the WAVEWATCH III model (WW3) and the other is the University of Miami Wave Model (UMWM). Within WW3, four different source term packages (ST2/3/4/6) of wind input, wave breaking dissipation and swell decay are chosen for comparison purposes. Based on the comparisons between model results and measurements from various platforms, we concluded that UMWM shows less accuracy than WW3 in specification of bulk wave parameters. This is possibly because (i) UMWM-estimated drag coefficient does not clearly show a saturation trend when wind speeds are beyond $\sim 35 \text{ m s}^{-1}$ and (ii) the four-wave interaction term of UMWM disagrees evidently with the full solution of the Boltzmann integral in detail. Among the four WW3 source term packages, the older parameterization ST2 is basically the least accurate because of its systematic underestimation of high waves. The remaining three packages (ST3/4/6) are performed well under Ivan. However, we also find that they tend to overestimate energy of waves traveling in the oblique and opposing winds. It is shown that enhancing the strength of negative wind input properly can effectively improve model skills in such situations. Limited by the uncertainty in the wind forcing, we could not determine the most accurate package among ST3/4/6 unambiguously.

© 2017 Elsevier Ltd. All rights reserved.

1. Introduction

Ocean surface waves subject to extreme weather conditions, such as hurricanes and extratropical storms, are of great interest to the oceanography and ocean engineering community (e.g., Young, 1999). Numerical simulations of hurricane- and storm-generated wave fields have been continuously studied for a number of decades (e.g., The WAMDI Group, 1988; Cardone et al., 1996; Moon et al., 2003; Babanin et al., 2011). As far back as 1980s, The WAMDI Group (1988) has demonstrated that the third generation (3G) spectral wave model can simulate wave heights under hurricane conditions reasonably as long as the driving wind forcing is accurate enough. Later in Cardone et al. (1996), the authors proved the slight advantage of 3G wave models over their previous counterparts (i.e., 1G and 2G wave models) on the basis

of two severe extratropical storm cases. Due to lack of measurements under extreme conditions, the assessment and validation of model performance typically relied on limited measurements from a few moored buoy stations or oil platforms, which generally cannot reflect the spatial patterns of wave fields very well. Using measurements acquired by scanning radar altimeter (SRA) under hurricane Bonnie (1998), Moon et al. (2003) were able to evaluate model skills in simulating spatial distribution of wave heights and spectral details. It was shown that the model spectra generally agree very well with SRA observations. Similarly, Fan et al. (2009b) compared their model results against SRA data under hurricane Ivan (2004) and clearly demonstrated the effect of currents on ocean waves. In addition, the influences of ocean waves on hurricane intensity forecasting were gradually recognized by operational meteorologists and the idea of fully coupled atmosphere-wave-ocean models began to be widely accepted (e.g. Chen et al., 2007; Warner et al., 2010).

* Corresponding author.

E-mail addresses: qingxiang.liu@unimelb.edu.au, qxiangliu@gmail.com (Q. Liu).

With respect to wave models alone, significant progresses have been made by the wave modelling community over the last 3 decades (e.g., Cavaleri et al., 2007; Tolman et al., 2013). To date, a number of 3G wave models have been developed (e.g., The WAMDI Group, 1988; Tolman, 1991; Booij et al., 1999; Roland, 2008; Donelan et al., 2012). Each model has been shown to work well under high wind regime conditions (e.g., Tolman et al., 2005; Dietrich et al., 2011; Montoya et al., 2013; Zieger et al., 2015; Chen and Curcic, 2015). From both the scientific and practical point of view, it is necessary to understand their relative strengths/weaknesses under extreme conditions. In this article, we choose the well-observed hurricane case Ivan (2004) (Fan et al., 2009b) as an example and inter-compare the performance of two wave models under hurricane conditions. One is the WAVEWATCH III model (WW3; Tolman and The WAVEWATCH III Development Group, 2014, hereafter T14) and the other is the University of Miami Wave Model (UMWM; Donelan et al., 2012). Within WW3, four different source term packages of wind input, wave breaking dissipation and swell decay are chosen for comparison purposes. Roughly speaking, these selections generally cover the most widely-used source term packages proposed in the literature.

This paper is organized as follows. Section 2 introduces the relevant information on Ivan (2004) and the reference data we collected from various platforms (SRA, satellite radar altimeter and buoy stations). Details pertaining to the driving wind forcing and wave models selected are also incorporated in this section. Section 3 presents the comparisons between measurements and model simulations. Section 4 offers further discussions on the model-estimated drag coefficient, the strength of negative wind input and the four-wave nonlinear interaction term. A brief conclusion in Section 5, together with the limitations of our study which primarily result from uncertainty in the wind forcing, finalizes this paper.

2. Data and methods

2.1. Hurricane Ivan (2004)

Hurricane Ivan (henceforth denoted as Ivan), occurring in the Caribbean Sea and Gulf of Mexico in September 2004, was a classical, long-lived, category 4–5 tropical cyclone on the Saffir–Simpson hurricane scale (Fig. 1). As of today, it remains one of the best-observed storms ever recorded in the Northern Atlantic Ocean (e.g., Wang et al., 2005; Black et al., 2007; Fan et al., 2009b). Due to its data-rich feature, Ivan has been extensively studied and simulated in the literature (e.g., Moon et al., 2007; Fan et al., 2009b; Smith et al., 2013; Fan and Rogers, 2016). Among them, Fan et al. (2009b) and Fan and Rogers (2016) carefully studied the sea state under Ivan by comparing model results against measurements from the National Aeronautics and Space Administration (NASA) scanning radar altimeter (SRA) (Wright et al., 2001).

2.1.1. In-situ buoy measurements

Three deep-water NDBC buoys (Fig. 1; red triangles) have been adopted for validating the driving wind forcing and the wave simulations. Each of them provides wind speed U_z (where the subscript z denotes the height above the sea level), wind direction θ_u and standard wave parameters (significant wave height H_s , mean wave period T_{02} and one-dimensional (1D) frequency spectra $E(f)$). Wind observations at non-standard heights (i.e., $z \neq 10$ m) were adjusted to be U_{10} by using the method detailed in Zieger et al. (2009). The only difference is that instead of using a constant drag coefficient C_d , we applied the parameterization proposed by Hwang (2011) and later modified by Rogers et al. (2012) (see the red solid line in our Fig. 9), which reads

$$C_d = \begin{cases} (-0.016U_{10}^2 + 0.967U_{10} + 8.058) \times 10^{-4} & \text{for } U_{10} < 50.33 \text{ m s}^{-1} \\ (u_*^c/U_{10})^2 & \text{for } U_{10} \geq 50.33 \text{ m s}^{-1} \end{cases} \quad (1)$$

where $u_*^c = 2.026 \text{ m s}^{-1}$ is the capped friction velocity for very high winds. It is noteworthy that the parameterization of C_d , suggested by Zijlema et al. (2012) and then implemented in the SWAN model (Booij et al., 1999), shows a changing trend of C_d very similar to Eq. (1) with a minor offset $\sim 3 \times 10^{-4}$ in their absolute values (purple dashed line in our Fig. 9).

2.1.2. Radar altimeter measurements

Radar altimeters (RAs) can also provide high-quality wave height measurements (H_s) and reliable wind observations (U_{10}) (e.g., Zieger et al., 2009; Liu et al., 2016a), which are very useful for studies on wave modelling (e.g., Tolman, 2002; Ardhuin et al., 2010; Zieger et al., 2015) and wave climate (e.g., Young et al., 2011; Liu et al., 2016b). Five altimeters, namely European Remote Sensing-2 (ERS-2), Environmental Satellite (Envisat), Geosat Follow-On (GFO), Jason-1 and the Ocean Topography Experiment (TOPEX), were operational during Ivan's lifetime. The quality-controlled, fully calibrated and validated multi-platform altimeter database developed in Zieger et al. (2009) was used in our study. Any 1-Hz record satisfying the following two criteria was considered to be useful (Fig. 1; yellow dashed lines):

- the 1-Hz records should be more than 100 km offshore;
- the spatial and temporal separation between the altimeter records and the hurricane centers should be less than 3° and 3 h.

These two criteria were chosen to exclude the land contamination and to meet the areal extent of the wind forcing we used (Section 2.1.4).

2.1.3. SRA measurements

During Ivan, the NASA scanning radar altimeter (SRA) was carried by the NOAA hurricane research aircraft and has collected three sets of two-dimensional (2D) wavenumber spectra in the vicinity of hurricane centers (Fig. 1; solid white lines). A total of 376 spectra was acquired during the first 4-h flight between 16:14 and 20:10 UTC 9 September. The second 5-h flight, spanning from 10:39 to 15:41 UTC 12 September, provided 456 spectra. The last 7.6-h flight between 20:08 UTC 14 September and 03:47 UTC 15 September resulted in 600 spectra. The SRA was designed primarily to measure the energetic part of the wave spectrum and cannot resolve wave components at frequencies beyond ~ 0.17 Hz. For more technical details on the SRA wave measurements, the reader is referred to Wright et al. (2001) and Fan and Rogers (2016).

Fig. 2 analyzes these SRA wave measurements in a detailed way as in Wright et al. (2001) and Moon et al. (2003). The spatial distribution of three wave parameters, including wave height (H_s ; colored points), peak wave length and direction (L_p and θ_p corresponding to the discrete peak of the 2D wavenumber spectrum; the gray radials), for the three sets of SRA measurements is presented in Fig. 2 (a–c), respectively. The patterns given by the SRA measurements are generally consistent with previous studies (e.g., Wright et al., 2001; Young, 2003; 2006; Black et al., 2007, among others). The sea states on the right side of the hurricane track are basically much rougher than those on the left side due to the fetch effect and the asymmetry of hurricane forcing (see also Fig. 2 of Young, 2003). In the right and left forward quadrants, waves are clearly propagated from a region right to the hurricane center. Waves in rear quadrants, particularly in the right-rear quadrant, however, are in general locally driven and therefore feature shorter wavelengths (see also Fig. 4 of Young, 2006). The SRA data also compare well with the sector-based idea proposed in

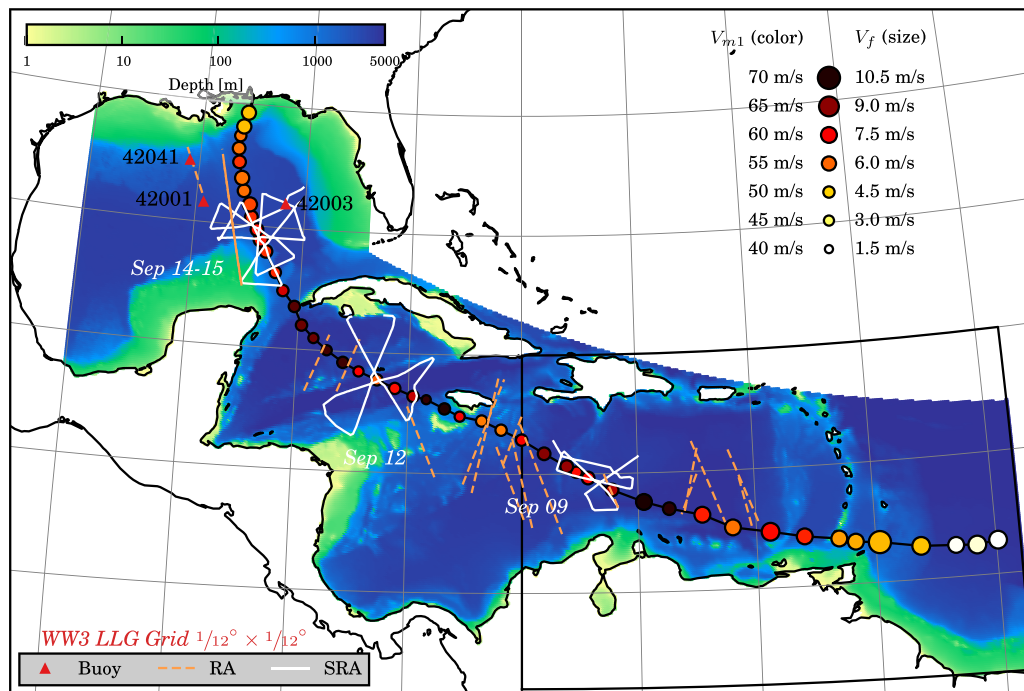


Fig. 1. The track (circles), maximum 1-min sustained wind speeds (V_{m1} ; color of circles) and translation speeds (V_f ; size of circles) of Hurricane Ivan (2004). Measurements from different platforms used in this study are also illustrated, including in-situ buoy (red triangles), radar altimeter (RA; yellow dashed lines) and scanning radar altimeter (SRA; white solid lines). The shaded contour plot shows the bathymetry of the $1/12^\circ \times 1/12^\circ$ longitude-latitude grid devised for wave models. The small domain bounded by the black box is used to obtain the optimal gust factor for each wave model (see Sections 2.1.4 and 2.2 for explanations). (For interpretation of the references to colour in this figure legend, the reader is referred to the web version of this article.)

Black et al. (2007) (black dashed lines in Fig. 2(a–c)) (see also related discussions on this topic in Hwang, 2016 and Hwang and Walsh, 2016).

Wind-wave misalignment is a very common phenomenon under hurricane conditions, especially in the left-rear quadrants of hurricane centers. Given the wind direction θ_u and the peak wave direction θ_p , the angle between wind and wave can be defined as $\Delta\theta_{uw} = \min(|\theta_u - \theta_p|, 360^\circ - |\theta_u - \theta_p|)$ ($\Delta\theta_{uw} \in [0^\circ, 180^\circ]$). Following Donelan et al. (1997) and Holthuijsen et al. (2012), we regarded wave conditions as wind sea (WS) or following swell (FS) when $\Delta\theta_{uw} \leq 45^\circ$, cross swell (CS) when $45^\circ < \Delta\theta_{uw} \leq 135^\circ$ and opposing swell (OS) when $\Delta\theta_{uw} > 135^\circ$. Young (2006) showed that in the left-rear quadrant $\Delta\theta_{uw}$ can be as large as 170° in his comprehensive buoy dataset. Holthuijsen et al. (2012) reanalyzed the SRA measurements under Hurricane Bonnie and found that in the near field (the radius r to the hurricane center is less than the radius of maximum winds R_m), the right-front, left-front and rear sectors of the hurricane center are dominated by FS, CS and OS, respectively (see their Fig. 4 and our Fig. 2(e)). In the region far from the center ($r \sim 3 - 4R_m$), CS exists almost everywhere. This is, however, not well-consistent with the results in Hu and Chen (2011), in which the authors showed similar patterns in the near and far fields (see their Fig. 2). We extracted wind information from the Hurricane wind analysis system (Powell et al., 1996; 1998) (see our Section 2.1.4) and checked the 1432 SRA spectra in Fig. 2(d, e). All the measurements are rotated and transformed into a normalized frame in which the hurricane is moving directly toward the north as in Young (2006). We found that these measurements can basically combine the two works by Holthuijsen et al. (2012) and Hu and Chen (2011) together, that is, CS is more prevalent in farther afield but WS/FS and OS are still detectable with the former two regimes mainly appearing in the right-rear quadrant and the latter existing in the left-rear quad-

rant (Fig. 2(d)). It should be noted that the CSs present in the left (weak) side of the hurricane track generally have $\Delta\theta_{uw}$ greater than 90° (purple points in Fig. 2 (d, e)), as contrasted with those CSs in the right (strong) side with $\Delta\theta_{uw} < 90^\circ$ (gray points in Fig. 2 (d, e)).

2.1.4. Wind field specification

High-quality wind forcing is crucial for the performance of numerical wave modelling (e.g., Janssen, 2004). The specification of wind fields for tropical cyclones is not a straightforward task (Cardone and Cox, 2009). Following Fan et al. (2009b), we adopted the wind data from the NOAA Hurricane Research Division (HRD) real-time hurricane wind analysis system (H*Wind; Powell et al., 1996; 1998) to drive our simulations. The H*Wind wind fields were issued every 3 or 6 h, with a grid resolution of 6 km and a spatial extent of $8^\circ \times 8^\circ$ around the hurricane center. To avoid the “spatial-aliasing” effect caused by the wind interpolation methodology implemented in the contemporary wave models (Tolman and Alves, 2005), we interpolated the original 3(6)-hourly H*Wind data into 0.5-h intervals as described in Moon et al. (2008) (their Section 4). Fan et al. (2009b) further extended this technique to the normalization method (hereafter NI; see their Fig. 2). When calibrated against buoy (Fig. 3) and altimeter measurements (Fig. 4), this extension however is proved to be not very necessary for the Ivan case (see the captions of these two figures) and hence not pursued in our study.

Another detail should be mentioned is that the H*Wind data (as presented in Figs. 3 and 4) are maximum sustained (1-min average) wind V_{m1} . The ocean surface, however, responds to wind stress over longer time scales (Powell et al., 1996). Thus, we should apply a gust factor G_f to convert V_{m1} to 10-min (or longer) average wind speeds V_{avg}^T (the superscript “T” represents the time scale for

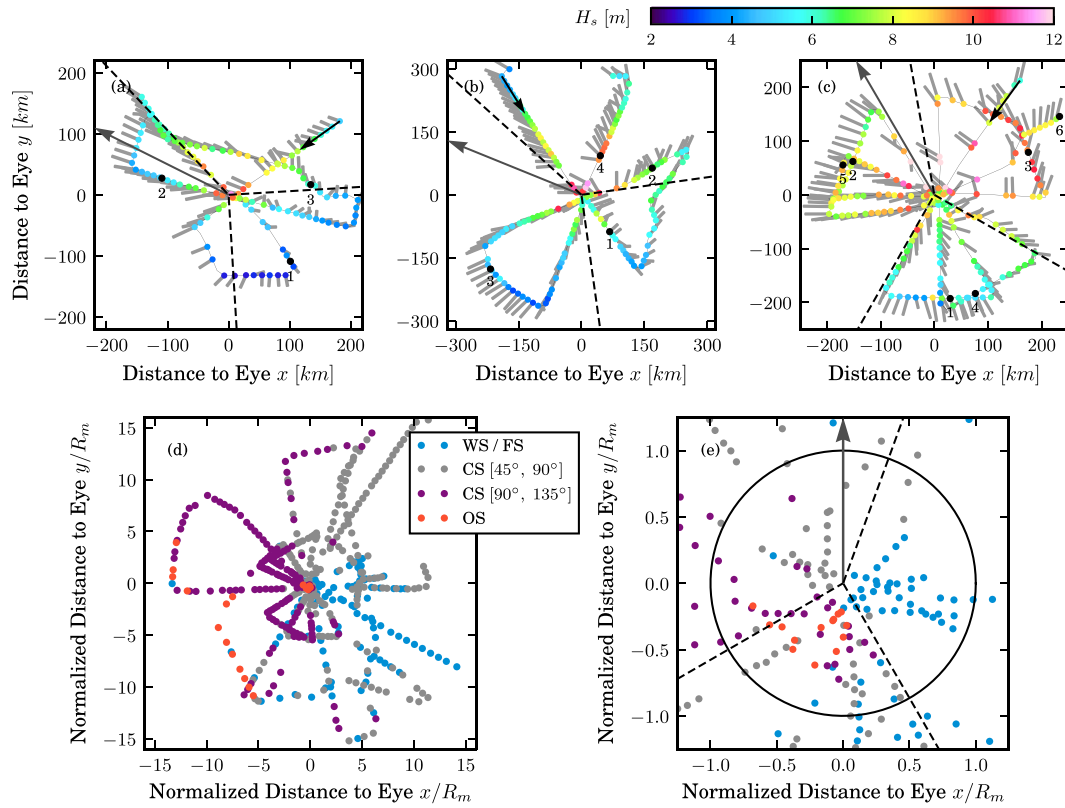


Fig. 2. SRA wave measurements obtained on (a) 9, (b) 12, and (c) 14–15 September 2004. The color of points represents wave height H_s , and the gray radials extend in the peak wave direction θ_p (the Cartesian convention) of which the length is proportional to the peak wave length L_p . The black and gray arrows indicate the starting points of the flight track and the mean direction of storm motion during the flight, respectively. The bigger black points and the number i below them highlight the i -hundredth SRA point. The x and y axis signify the relative distance of measurement locations to the *instant* hurricane centers. In panel (d), all the 1432 SRA measurements are assembled and transformed into a normalized frame in which the hurricane is moving directly toward the north as in Young (2006). Different colors denote different wave conditions: blue for wind sea or following swell (WS / FS), gray for cross swell (CS) with $\Delta\theta_{uw} \in [45^\circ, 90^\circ]$, purple for CS with $\Delta\theta_{uw} \in [90^\circ, 135^\circ]$ and red for opposing swell (OS). Panel (e) is a zoomed-in view of regions near the radius of maximum winds (R_m ; black circle). Except in panel (e), only every third SRA data point is presented for clarity. The three sectors proposed in Black et al. (2007) are also overlapped when necessary. (For interpretation of the references to colour in this figure legend, the reader is referred to the web version of this article.)

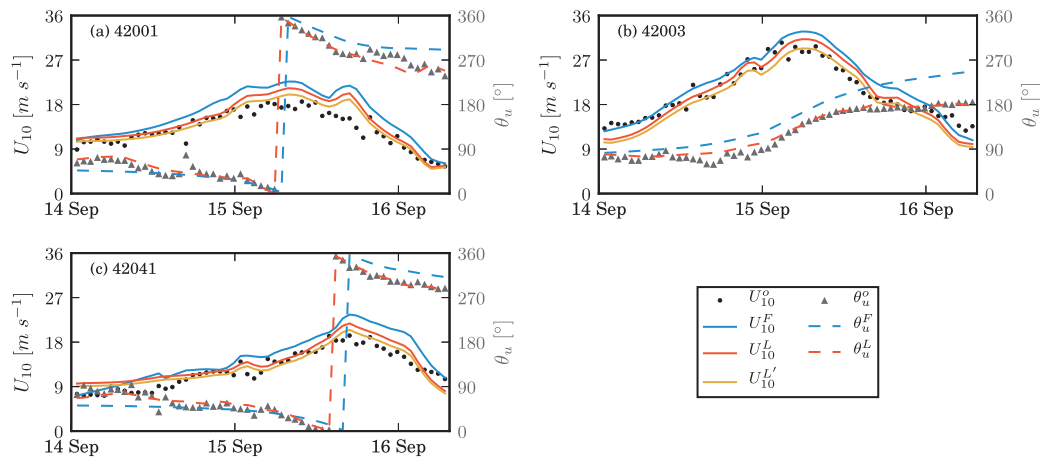


Fig. 3. Comparisons of (left y-axis) wind speed U_{10} and (right y-axis) wind direction θ_u between the hourly H*Wind data and NDBC buoy observations at (a) 42001, (b) 42003 and (c) 42041. The superscript in the legend means: o for buoy observations (black dot \bullet and gray triangle Δ); F for the processed H*Wind data from Fan et al. (2009b) which used the NI approach (blue solid and dashed lines); L for the processed H*Wind data used in this paper (red solid and dashed lines). It is clear that NI gives a stronger U_{10} and a less accurate θ_u . U_{10}^L , as represented by the yellow line, is the reduced U_{10}^L to minimize the RMSE between HRD data and buoy measurements (see text for more details). (For interpretation of the references to colour in this figure legend, the reader is referred to the web version of this article.)

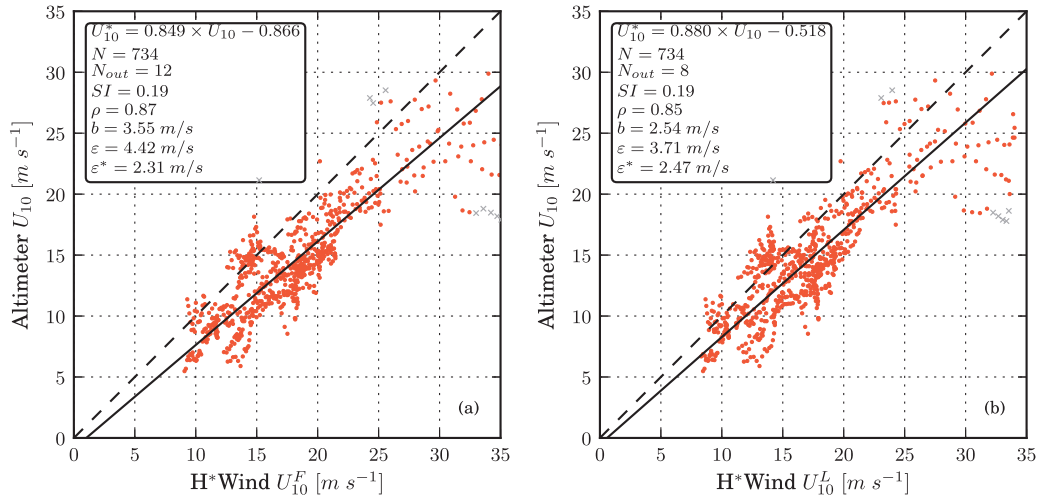


Fig. 4. Comparison between altimeter U_{10} measurements and the H*Wind data. U_{10}^f in panel (a) indicates the NI-generated wind data from Fan et al. (2009b) and U_{10}^l in panel (b) denotes the wind data used in this paper. The processed $1/12^\circ$, 0.5-hourly H*Wind data were interpolated bilinearly in space and linearly in time to the altimeter space-time location. The solid line represents the reduced-major-axis (RMA) fit and the dashed line is 1:1 line. Error statistics for scatter index (SI), correlation coefficient ρ , bias b , root-mean-square error (RMSE) ε and number N of sample points are given in the inset, with outliers N_{out} (detected by robust regression) labelled with gray crosses. The ε^* signifies the RMSE after the RMA correction. For the technical details, please refer to Zieger et al. (2009) and Liu et al. (2016a). Comparison between panel (a) and (b) shows that U_{10}^f is on average 1 m s^{-1} higher than U_{10}^l .

average) by

$$V_{avg}^T = V_{m1}/G_f^T, \quad (2)$$

as suggested in Powell and Houston (1996) and Powell et al. (2010). The conversion as formulated in Eq. (2) and the value of G_f and T , however, are not unambiguously defined. For example, Powell et al. (1996) and Powell and Houston (1996) recommended ($T = 10 \text{ min}$, $G_f^{10} = 1.11$) as a representative setting for the storm surge and wave models, which has been followed by Tolman et al. (2005) and Arduin et al. (2010). While recently in Powell et al. (2010), the authors advocated using a stronger reduction as ($T = 30 \text{ min}$, $G_f^{30} = 1.235$). A wind speed-dependent G_f was also used within the H*Wind analysis system (Eqs. (4)–(5) in Powell et al., 2010). To avoid such ambiguity, we resorted to find an optimal G_f , denoted as G_f^o , to minimize the root-mean-square error (RMSE, ε) between V_{avg}^T and U_{10} measured by NDBC buoys and radar altimeters. However, we found that it was impossible to collapse the two different kinds of observations with one single value of G_f^o . The buoy-estimated U_{10} favors $G_f^o = 1.06$ (yellow lines in Fig. 3), while the altimeter-sensed U_{10} supports $G_f^o = 1.19$ (Fig. 4 (b)). This will be further discussed in the next section. Moreover, it has to be kept in mind that due to their smoothness, the H*Wind data are not capable of resolving the band/eyewall structure changes of hurricanes (e.g., the eyewall replacement, see Sitkowski et al., 2011). It is not clear yet to what extent such uncertainty in the wind forcing impacts our wave model results.

2.2. Spectral wave modeling

The third generation (3G) spectral (or phase averaging) wave model (e.g., Komen et al., 1994; Young, 1999; Janssen, 2004; Holthuijsen, 2007) solves the radiative transfer equation (RTE) to predict the generation, evolution and dissipation of ocean surface waves. In a general framework, when the background current velocity is not zero, the RTE can be written as

$$\frac{dN}{dt} = \frac{S_{in}(+S_{swl}) + S_{ds} + S_{nl} + \dots}{\sigma}, \quad (3)$$

where $N(k, \theta; \mathbf{x}, t) = F(k, \theta; \mathbf{x}, t)/\sigma$ is the wave action density spectrum, $F(k, \theta; \mathbf{x}, t)$ is the wavenumber-direction spectrum, σ is the intrinsic (radian) frequency. The terms in the RHS of Eq. (3) signify the sources and sinks of wave energy due to various physical processes. Basically, S_{in} represents the wave growth or attenuation as a result of normal stress variations exerted on the water surface by the wind (e.g., Janssen, 1991; Chalikov and Belevich, 1993; Donelan et al., 2006; Kahma et al., 2016), S_{ds} signifies the dissipation due to wave breaking (e.g., Komen et al., 1984; Tolman and Chalikov, 1996; Arduin et al., 2010; Babanin et al., 2010), S_{nl} redistributes energy over the spectrum because of nonlinear four-wave interactions (Hasselmann, 1962) and S_{swl} is the so-called swell (or non-breaking) dissipation term. The mechanisms responsible for S_{swl} are not clearly understood yet. They may either be formulated as negative wind input (e.g., Tolman and Chalikov, 1996; Donelan et al., 2012; Zieger et al., 2015) or be parameterized explicitly to export a flux of energy from waves to the air (Arduin et al., 2009; 2010) or to the sea (Babanin, 2006; 2011; Zieger et al., 2015). Other processes changing the wave energy in shallow water for example have been omitted in Eq. (3). The reader is referred to Young (1999), Cavaleri et al. (2007) and Holthuijsen (2007) for extensive discussions on those topics. An updated review of the current status and perspectives of the ocean surface wave research can also be found in Babanin et al. (2012).

As we already mentioned in the Introduction, we used two wave models to hindcast Ivan. One is the widely used 3G wave model WW3 (T14) and the other is UMWM (Donelan et al., 2012) (version 1.0.1). UMWM was devised as an efficient wave model to provide full atmosphere-wave-ocean coupling in hurricane forecasting systems (Chen and Curcic, 2015). Thus, the physics-based but time-consuming source term S_{nl} (e.g., Hasselmann et al., 1985; van Vledder, 2006; Tolman, 2013) was treated parametrically in such a way that wave breaking was assumed to be the primary cause of the shift of energy to the longer waves (Donelan et al., 2012). Within the modeling framework of WW3, various parameterizations of $S_{in}(+S_{swl}) + S_{ds}$ have been implemented on the basis of different perceptions of related physics. Four source term packages for $S_{in}(+S_{swl}) + S_{ds}$ have been selected in this paper, denoted as ST2 (Chalikov and Belevich, 1993; Tolman and Chalikov, 1996; Tolman, 2002), ST3 (Janssen, 1991; 2004; Bidlot et al.,

Table 1

Model setup, including frequency (f_i) and direction ($\Delta\theta$ and N_θ) grid, domain size and resolution, numerical approach and different source terms ($S_{in} (+S_{swl}) + S_{ds}$, S_{nl}). The model attributes presented in the second column are shared by all the five models unless otherwise specified. The two-row brackets emphasize the different time steps and numerical schemes used by four WW3-type models (labeled with \mathcal{W}) and UMWM (labeled with \mathcal{U}). In column S_{nl} , † identifies DIA approach used in WW3, after which the proportionality constant C of DIA is also presented (see e.g. Eq. (5.5) of Hasselmann et al., 1985). In the last column, we highlighted the key tuning parameters of each model and related references.

Model	Model setup	$S_{in} (+S_{swl}) + S_{ds}$	S_{nl}	Tuning Parameters
WW3-ST2	Frequency and Direction grid: $f_i = f_1 \times 1.1^{i-1}$, $i = 1, \dots, 35$ $f_1 = 0.0373$, $f_{35} = 0.9529$ $\Delta\theta = 10^\circ$, $N_\theta = 36$	Chalikov and Belevich (1993) Tolman and Chalikov (1996) Tolman (2002)	† $C = 1.00 \times 10^7$	Tolman (2002) $C_{d,max} = 2.5 \times 10^{-3}$
WW3-ST3	Domain grid: 95°W – 54°W, 6°N – 30.5°N, 1/12° × 1/12°	Janssen (1991) Janssen (2004) Bidlot et al. (2007) Bidlot (2012)	† $C = 2.78 \times 10^7$	Bidlot (2012) T14
WW3-ST4	Time step: \mathcal{W} : 600, 300, 300, 30 s \mathcal{U} : dtg = 600 s	Ardhuin et al. (2009) Ardhuin et al. (2010) Leckler et al. (2013)	† $C = 2.50 \times 10^7$	TEST451: $\beta_{max} = 1.52$ $S_u = 1$ $z_{0,max} = 1.002$
WW3-ST6	Numerical Scheme: \mathcal{W} : Third order (UQ) \mathcal{U} : First order upstream	Donelan et al. (2006) Babanin (2011) Rogers et al. (2012) Zieger et al. (2015)	† $C = 3.00 \times 10^7$	Zieger et al. (2015) CSTB1 = .F
UMWM		Donelan et al. (2012)	induced by S_{ds}	Donelan and Curcic (2012)

2007; Bidlot, 2012), ST4 (Ardhuin et al., 2010; Leckler et al., 2013) and ST6 (Donelan et al., 2006; Babanin, 2011; Rogers et al., 2012; Zieger et al., 2015). For the detailed description of each package, the reader is referred to T14 and references therein. A brief summary of these four packages has also been presented in Stopa et al. (2016), in which the authors inter-compared them on the basis of one-year global hindcast. For WW3, the discrete interactive approximation approach (DIA; Hasselmann et al., 1985) is employed to compute the nonlinear four-wave interactions (S_{nl}), unless otherwise specified differently. Same as UMWM, hereafter each source term package of WW3 will be referred to as an independent wave model for convenience.

Another detail related to the simulation of hurricane-induced waves is how to parameterize the drag coefficient (and wind stress) under high wind speed conditions within the wind input source term S_{in} . It has been shown through field measurements (Powell et al., 2003; Jarosz et al., 2007; Holthuijsen et al., 2012), laboratory experiments (e.g., Donelan et al., 2004; Takagaki et al., 2012) and theoretical studies (e.g., Moon et al., 2004; Soloviev et al., 2014) that the drag coefficient C_d qualitatively tends to level off or even decrease when U_{10} exceeds $\sim 33 \text{ m s}^{-1}$. However, there is no consensus yet on how C_d changes quantitatively under such regime. Different source term packages also treat C_d in different ways. In ST2, C_d is capped with a maximum allowed drag coefficient $C_{d,max}$ (T14), consistent with the pioneering work by Khandekar et al. (1994). Similarly, ST4 uses a capped aerodynamic roughness length $z_{0,max}$ to “reduce possible unrealistic wind stresses at high winds” (Ardhuin et al., 2010). At the same time, the wind-sheltering effect formulated in the S_{in} function of ST4 plays a similar role in limiting the roughness to $z_{0,max}$ (see Eq. (24) and Fig. 14 of Ardhuin et al., 2010). ST6 chooses Eq. (1) to account for the saturation and decrease of C_d for extreme winds (Rogers et al., 2012; Zieger et al., 2015). In addition, S_{in} of ST6 (Donelan et al., 2006) is dependent on wave slope and degree of air-sea flow separation. For very strong wind forcing a condition of so-called full separation occurs and consequently momentum fluxes injected into waves by winds are generally weaker relative to non-separated regime. This novel feature of S_{in} is also believed to be a possible mechanism that contributes to the levelling off of

C_d under high winds. Unlike other models, ST3¹ and UMWM do not implement any limits on C_d .

The detailed setup (frequency and direction grid, domain size and resolution, numerical approach, tuning parameters etc.) of each wave model is summarized in Table 1. Unnecessary waters beyond the Caribbean Sea and Gulf of Mexico were excluded in our simulations to reduce the computational expense (Fig. 1). Fan et al. (2009a; 2009b) found from their simulations that the current-induced advection and refraction of wave energy can play a very important role in the modulation of wave fields under hurricane conditions. Particularly in the right-forward quadrant of the hurricane center where the currents are strong and roughly aligned with the dominant wave propagating direction, the advection effect of currents can introduce an absolute (relative) error in H_s as large as 2 m ($\sim 20\%$) (see Fan et al., 2009b, their Section 5.b and Fig. 11 for example). Thus, except the wind forcing from Section 2.1.4, we also used the ocean surface currents from the HYCOM+NCODA Global 1/12° Analysis dataset (Cummings, 2005; Cummings and Smedstad, 2013) to account for the current effects.

As mentioned in Section 2.1.4, we failed to find a consistent gust factor G_f^o . Consequently, we decided to firstly make an attempt to find another optimal G_f , denoted as G_f^m , to minimize the RMSE between the model-simulated H_s and the SRA-observed H_s from its first 4-h flight (Fig. 2 (a)). This was undertaken by only running wave models in a subregion of our 1/12° × 1/12° domain (the region inside the black box in Fig. 1). The simulation period spans from 1930 UTC 6 September to 0130 UTC 10 September 2004. Only the first set of SRA measurements was chosen because Fan et al. (2009b) and Fan and Rogers (2016) showed that their model results agreed best with this set of SRA data. It is not surprising that we obtained different values of G_f^m for different wave models² (see Table 2). After G_f^m was determined, we re-ran the wave model with the full domain and then compared the model output

¹ Bidlot (2012) reported that “a bug in the determination of total stress in WAM was introduced” in April 2005, which resulted in an artificial capping of C_d for high winds (see their Section 2.9 and Fig. 3). Unfortunately, this bug was reproduced when ST3 was imported from WAM into WW3.

² Alternatively, we can also try to optimize the tunable parameter which controls the strength of S_{in} of each model, such as u_c in ST2, β_{max} in ST3 and ST4, CDFAC

Table 2

Error metrics for the model-data comparisons. In the second column, G_f^m is the optimal gust factor which minimizes the RMSE ε between the model simulated H_s and the SRA-observed H_s from its first 4-h flight (see Sections 2.1.4 and 2.2). The corresponding optimal bias b^{H_s} (m) and RMSE ε^{H_s} (m) are also indicated in the following bracket. Comparisons between the full-domain simulations and all the available data are presented in the remaining columns. Three bulk parameters, namely wave height H_s (m), mean wave direction θ_w ($^\circ$) and wave period T_{02} (s) and four error statistics, including bias b , RMSE ε , correlation coefficient ρ and scatter index SI are chosen to quantify the skill of different source term packages. The definition of each parameter can be found in Appendix A. The best metrics given by the five models are shown in **bold**.

Model	H-Wind U_{10} G_f^m (b^{H_s} , ε^{H_s})	SRA								RA							
		H_s [m]				θ_w [$^\circ$]				T_{02} [s]				H_s [m]			
		b	ε	ρ	SI	ε	b	ε	ρ	SI	b	ε	ρ	SI			
WW3-ST2	1.08 (0.00, 1.08)	-0.51	1.22	0.86	0.16	32.6	-0.49	0.85	0.68	0.07	-0.28	0.99	0.89	0.20			
WW3-ST3	1.16 (0.03, 1.16)	0.13	1.09	0.87	0.15	24.9	-0.06	0.54	0.80	0.05	-0.11	0.91	0.90	0.19			
WW3-ST4	1.14 (-0.03, 1.09)	0.49	1.28	0.86	0.17	25.1	0.15	0.58	0.79	0.06	0.05	0.87	0.91	0.18			
WW3-ST6	1.16 (0.00, 1.04)	0.32	1.09	0.87	0.15	23.4	-0.09	0.56	0.78	0.06	0.07	0.84	0.91	0.17			
UMWM	1.16 (0.00, 1.78)	0.71	2.16	0.75	0.29	25.6	-0.07	0.85	0.59	0.09	-0.86	1.41	0.87	0.23			
Buoy																	
H_s [m]																	
T_{02} [s]																	
b ε ρ SI b ε ρ SI																	
WW3-ST2		-0.95	1.32	0.93	0.17	-0.87	1.20	0.75	0.10								
WW3-ST3		-0.79	1.03	0.96	0.13	-0.49	0.82	0.86	0.08								
WW3-ST4		-0.51	0.82	0.96	0.12	-0.26	0.78	0.82	0.09								
WW3-ST6		-0.52	0.91	0.95	0.14	-0.51	0.93	0.78	0.10								
UMWM		-1.40	1.77	0.89	0.20	-1.22	1.44	0.85	0.10								

with all the measurements detailed in Section 2.1. All the full simulations started from 1930 UTC 6 September and ended at 0730 UTC 16 September 2004.

3. Conventional model analysis

A sensitivity study on the gust factor G_f^m yields an optimal value for each model as listed in Table 2 (the second column). The G_f^m for ST2 is the lowest (1.08), close to the buoy-estimated value (1.06); while the four other models correspond to higher values (1.14 for ST4 and 1.16 for ST3, ST6 and UMWM), approximating to the value derived from the altimeter data (1.19). It should be remembered that a higher G_f^m means a stronger reduction of the original H*Wind data. From those five different values of G_f^m , it is clear that under high wind conditions ST2 is less energetic than the others (see also Fig. 17 of Zieger et al., 2015).

3.1. Comparison against SRA measurements

The detailed comparisons between SRA observations and model simulations are presented in Fig. 5; corresponding error metrics are summarized in Table 2 and Fig. 8. The SRA wavenumber spectrum $F(k_x, k_y)$ was converted into 2D frequency-direction spectrum $F(f, \theta)$ through the following Jacobian transformation (e.g., Young, 1999):

$$F(f, \theta) = \frac{2\pi |\mathbf{k}|}{c_g} F(k_x, k_y), \quad (4)$$

where $|\mathbf{k}|$ is the magnitude of the wavenumber vector. Three integral parameters (integral range across frequencies from 0.037 Hz to 0.17 Hz, the highest frequency that the SRA can resolve), namely significant wave height H_s , mean wave direction θ_w ³ and mean wave period T_{02} (see Appendix A), are chosen to evaluate the model skill. In our case, the relative model performances

in ST6 and explim in UMWM. For example, Fan and Rogers (2016) decreased β_{\max} of ST4 from its default value 1.52 to 1.28.

³ The mean wave direction θ_w is slightly more stable than the peak wave direction θ_p and is therefore adopted in the comparison.

of other measures for wave period, such as T_{m01} and $T_{m-1,0}$ (Holthuijsen, 2007), is similar to that of T_{02} and thus are not included here.

In general, once the optimal gust factor G_f^m is applied, all the five models are capable of estimating the observed sea states (H_s) reasonably (Fig. 5 (a, d, g, j)). The bias (b) varies from -0.51 m for ST2 to 0.71 m for UMWM. Biases for the three other models are less than 0.5 m, and ST3 is the least biased ($b = 0.13$ m). The RMSE (ε) varies from 1.09 m for ST3 and ST6 to 2.16 m for UMWM. RMSEs of ST2 and ST4 (~ 1.25 m) are slightly higher than those of ST3 and ST6. The correlation coefficients of WW3-type models (i.e., ST2/3/4/6) are in between 0.86 and 0.87, higher than that for UMWM ($\rho = 0.75$). Similarly, all the four WW3-type models characterize very close scatter index SI (0.15–0.17), which is relatively small compared to the value for UMWM (0.29). As revealed by the four statistical parameters, UMWM is not as good as those WW3-type models in specification of H_s in Ivan. This is also apparently illustrated by the Taylor diagram (Taylor, 2001) in Fig. 8 (a) (full markers with black edge line). From Fig. 5 (a, d, g, j), we know that UMWM tends to underestimate wave heights smaller than 5 m and conversely overestimates high waves, especially for $H_s > 10$ m. Besides, UMWM cannot reproduce well the decline trend of H_s in the vicinity of hurricane eyes. Taking the flight fragment Point 200–250 obtained on September 12 as an example (Fig. 2 (b)), the aircraft was proceeding southwestward from the right side of the hurricane center to the left side. The observed H_s decreased from its local maximum of ~ 11 m to its local minimum of 6 m, and then increased to another local maximum around 10 m again (black dots in Fig. 5 (d)); while the UMWM-hindcasted H_s is always above 10 m during this particular period (gray line in Fig. 5(d)). Similar overestimations of waves near the hurricane centers are also common when UMWM results are compared against the third set of SRA observations (Figs. 2(c) and 5 (g, j)). According to the statistical skills mentioned above and detailed in Table 2, among the four WW3-type models, ST3 and ST6 outperform ST2 and ST4 slightly. The Taylor diagram in Fig. 8(a) (full markers with black edge line) shows all the models overestimate the variability of the observed H_s , with ST6 being the least biased. One detail should be stressed is that it is obvious from Fig. 5 (d, g, j) that ST2

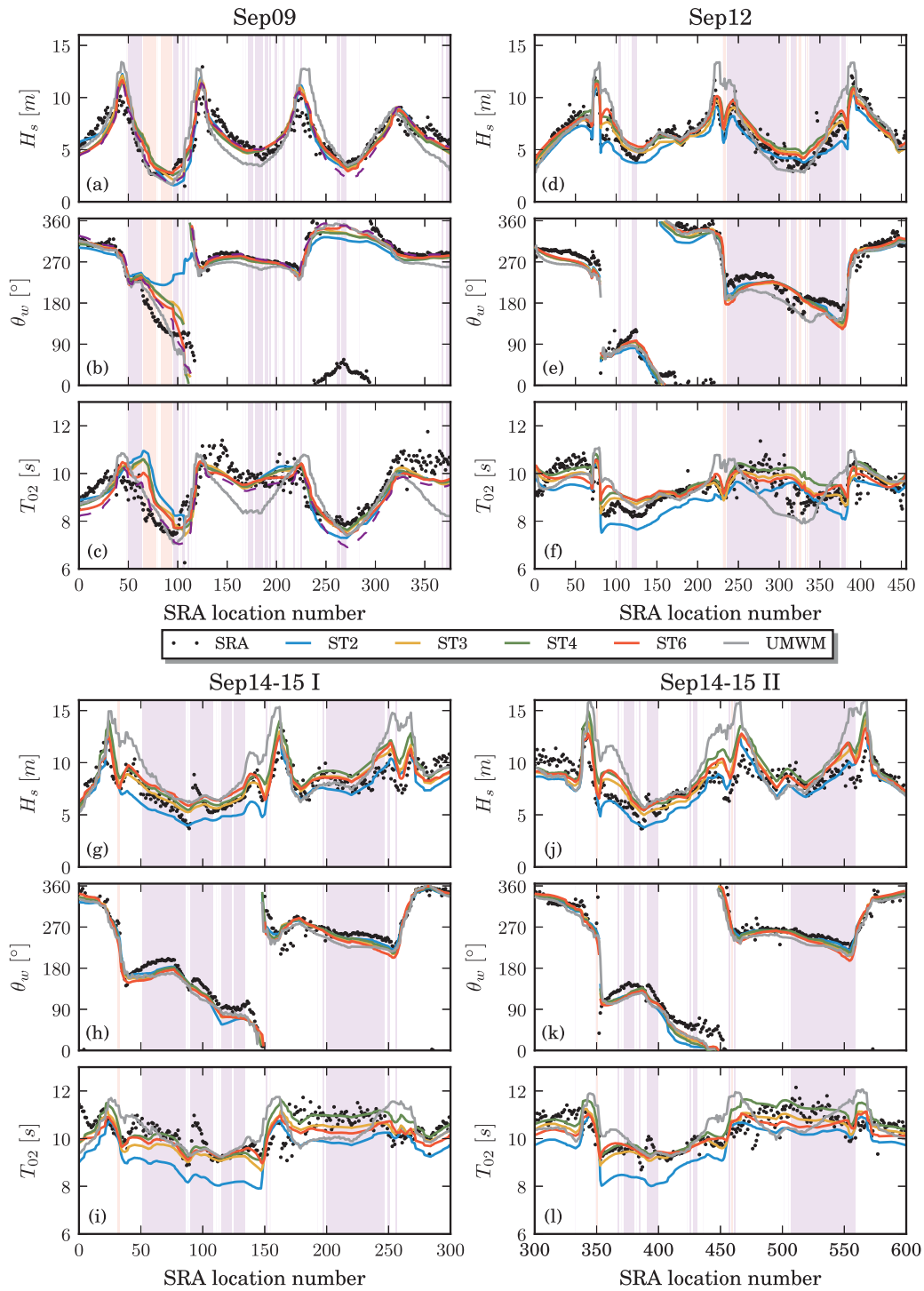


Fig. 5. Comparison of model results (colored lines: blue for ST2, yellow for ST3, green for ST4, red for ST6 and gray for UMWM) and SRA observations (black dot •) acquired on September (a–c) 9, (d–f) 12 and (g–l) 14–15. For clarity, the third set of SRA measurements is divided into two parts. One (the first 300 records) is plotted in panels (g–i) and the other (the remaining 300 records) in panels (j–l). Three bulk parameters are taken into account: (a, d, g, j) significant wave height H_s , (b, e, h, k) mean wave direction θ_w (oceanographic convention: the direction towards which waves are propagating, measured clockwise from geographic North) and (c, f, i, l) mean wave period T_{02} . The purple dashed lines in panel (a–c) represent the results from the ST6+WRT experiment. The purple (red) shaded region highlights CSs with $\Delta\theta \in [90^\circ, 135^\circ]$ (OSs) as detected in Fig. 2. (For interpretation of the references to colour in this figure legend, the reader is referred to the web version of this article.)

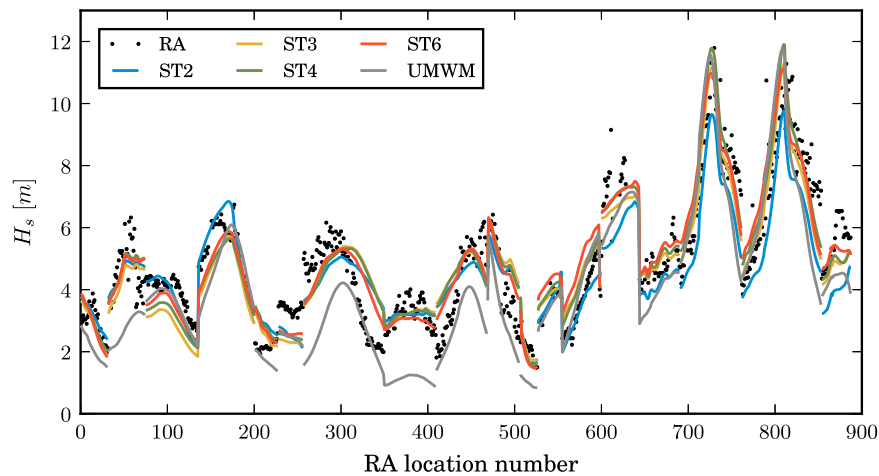


Fig. 6. Wave height H_s observed by RA (black dot: •) and simulated by wave models (colored lines: blue for ST2, yellow for ST3, green for ST4, red for ST6 and gray for UMWM). The 1-Hz RA measurements are sorted by time as presented in the horizontal axis. (For interpretation of the references to colour in this figure legend, the reader is referred to the web version of this article.)

tends to give the lowest H_s . Given the fact that the wind forcing for ST2 is 5% (7%) stronger than that for ST4 (ST3/ST6/UMWM), it is reasonable to draw a conclusion that ST2 has problems in predicting extreme wave events.

All the five models also provide reasonable mean wave direction θ_w (Fig. 5(b, e, h, k)). Except for the two particular segments (Point 60–100 and Point 250–300)⁴ from the first SRA flight (Fig. 5 (b)), all models are able to hindcast θ_w reasonably well. In terms of θ_w , only the metric RMSE (ε) is statistically meaningful (see Appendix A). The lowest ε of 23.4° is given by ST6, closely followed by ST3, ST4 and UMWM with $\varepsilon \sim 25^\circ$. The maximal ε of 32.6° was seen in the ST2 experiment.

Unlike H_s and θ_w , differences among the models in estimating the mean wave period T_{02} are slightly more apparent. Except ST4, all the four other models show a negative bias for T_{02} . Periods given by ST2 are the most biased, which on average are 0.49 s lower than observations. ST3, ST6 and UMWM underestimate T_{02} marginally ($|b| < 0.1$ s); while ST4 overestimates T_{02} by 0.15 s. The minimum RMSE ($\varepsilon = 0.54$ s) is provided by ST3, closely followed by ST6 and ST4 (0.56 s and 0.58 s), with ST2 and UMWM featuring the highest ε (0.85 s). Similarly, from the correlation coefficients ρ and scatter index SI , we know that ST3, ST4 and ST6 provide similar performances in computing wave periods, and each of them is notably outperforming ST2 and UMWM. Inspection of Fig. 5 (c, f, i, l) shows that ST2 tends to underestimate wave period quite often, contributing to its high RMSE of T_{02} . This is a known deficiency of ST2 mainly because of its reduced DIA strength⁵ (Tolman, 2010, his Fig. 3.1). UMWM is slightly worse than ST2, as represented by the lower ρ and higher SI . The Taylor diagram in Fig. 8 (b) shows that UMWM overestimates the measured variability of T_{02} , whereas others underestimate that in some degree. In this regard, ST4 is slightly better than ST3 and ST6, although their model skills as identified by the four metrics are very close.

⁴ This mismatch between models and SRA observations is possibly resulted from the inaccurate wind directions. Fan et al. (2009b) used the NI approach (see Section 2.1.4) to process the H⁺Wind data and obtained better model-SRA agreement for these two fragments than ours (see their Fig. 4 (b)).

⁵ The proportionality constant of DIA adopted by ST2 is $C = 1.0 \times 10^7$, which is quite lower than the values used by ST3/4/6 ($C \geq 2.5 \times 10^7$) (see e.g. the fourth column of our Table 1).

3.2. Comparison against RA measurements

The detailed comparison between the RA-observed H_s and the model-estimated H_s is presented in Fig. 6. The results are basically similar to what we have seen in Fig. 5 (a, d, g, j). ST2, ST3 and UMWM show a negative bias in H_s , spanning from -0.86 m for UMWM to -0.11 m for ST3. In contrast, ST4 and ST6 provide marginally positive biases (0.05 m and 0.07 m). The RMSE varies from 0.84 m for ST6 and 1.41 m for UMWM. The correlation coefficients for ST4 and ST6 are highest (0.91), and UMWM shows the lowest ρ of 0.87. The smallest SI (0.17) appears in the ST6 experiments. This is very close to ST3/4-provided values, whereas ST2 and UMWM remain as the most two scattered models. Once again, these error metrics, together with the Taylor diagram in Fig. 8 (a) (markers without edge line), clearly reveal that ST2 and UMWM are not as accurate as three other models. As in Fig. 5, here ST2 generally gives lower H_s than others when $H_s > 6$ m, and UMWM underestimates low wave heights ($H_s < 5$ m) significantly.

3.3. Comparison against buoy measurements

We compared our model results with measurements from the three deep-water NDBC buoys in Fig. 7. In this case, the wave height H_s and wave period T_{02} are concerned. Unlike the previous comparisons, all the models systematically underestimate the buoy-observed values to some extent. For H_s , models show the highest accuracy at station 42003 (Fig. 7 (c)). However, apart from ST4 and UMWM, all the others apparently underspecify the peak values by about 2–3 m. The drawback of missing peak sea states is also clearly seen at the two other buoys (Fig. 7 (a, e)). Besides, at stations 42001 and 42041, all the models lag the increase of H_s by around 3–6 h. Looking at the error metrics summarized in Table 2, ST2 and UMWM remain as the most two biased models ($b = -0.95$ m and $b = -1.40$ m, respectively). ST4 appears to be the best model in matching the buoy observed H_s and T_{02} . The skills of ST3 and ST6 are quite close. However, from the Taylor diagram (Fig. 8 (b), hollow markers), we can see that the variability of T_{02} is again underestimated by ST6.

We note that the underestimation of H_s and T_{02} , as seen in Fig. 7, possibly resulted from the imbalanced accuracy of wind forcing at buoy locations and SRA trajectories. The values of G_f^m were specified for ST3, ST4, ST6 and UMWM (favored by SRA records)

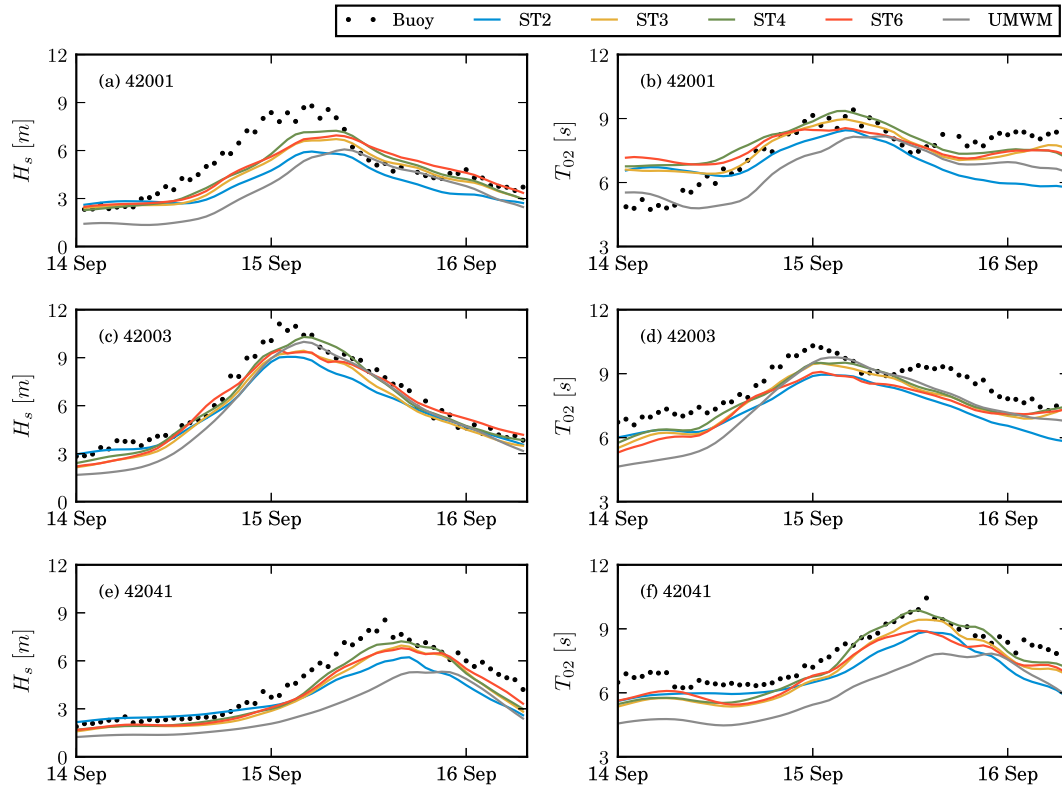


Fig. 7. Comparison of (left) wave height H_s and (right) wave period T_{02} between model values (colored lines as in Figs. 5 and 6) and buoy measurements (black dot \bullet) at station (a, b) 42001, (c, d) 42003 and (e, f) 42041. (For interpretation of the references to colour in this figure legend, the reader is referred to the web version of this article.)

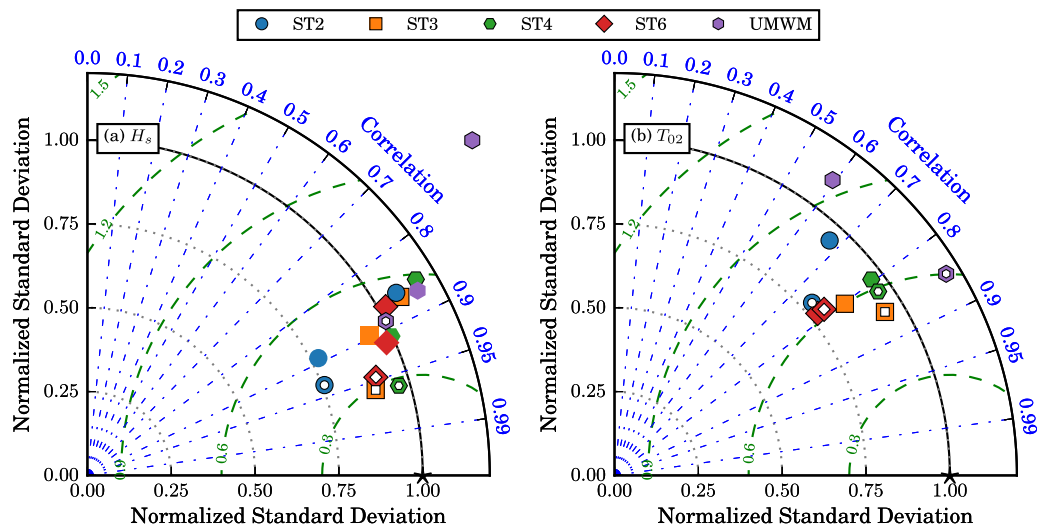


Fig. 8. Taylor diagrams summarizing statistical comparisons of (a) wave height H_s and (b) wave period T_{02} between model results (blue circle: ST2, yellow square: ST3, green hexagon: ST4, red diamond: ST6 and purple hexagon: UMWM) and observations from different platforms (full markers with black edge line: model vs. SRA; full markers without edge: model vs. RA; hollow markers: model vs. buoy). (For interpretation of the references to colour in this figure legend, the reader is referred to the web version of this article.)

are obviously greater than the buoy-favored one (1.14 and 1.16 vs. 1.06). Consequently, the actual wind speeds driving these four wave models are approximately 6–8% lower than buoy-observed U_{10} . Given the larger sample size of SRA-model collocations and their better agreement, we will concentrate on using SRA wave spectra only in the following discussion sections.

4. Additional discussion

4.1. Drag coefficient C_d

We have mentioned briefly in Section 2.2 that each wave model parameterizes C_d and therefore u_* differently. Considering the di-

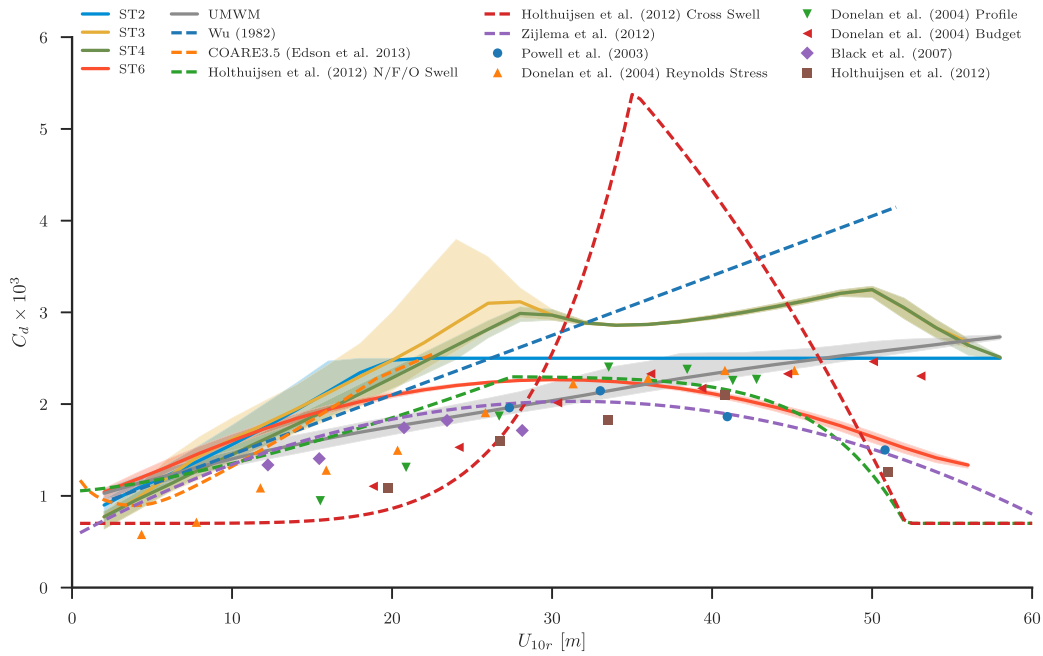


Fig. 9. Drag coefficient (C_d) as a function of relative wind speed U_{10r} , adapted from Fig.6(a) of Holthuijsen et al. (2012). The model-estimated C_d are averaged into 2 m s^{-1} bins of U_{10r} and shown in solid lines, around which the shaded region illustrates the C_d values in between the 5th and 95th percentiles for each 2- $m s^{-1}$ U_{10r} bin. Parameterizations of C_d proposed by Wu (1982), Edson et al. (2013) (i.e., COARE3.5 algorithm), Holthuijsen et al. (2012) and Zijlema et al. (2012) (dashed lines) and laboratory and field measurements from Powell et al. (2003), Donelan et al. (2004), Black et al. (2007) and Holthuijsen et al. (2012)(markers) are also shown for comparison. The ocean surface current velocity was assumed to be zero when relevant information was not available. It should be noted that Holthuijsen et al. (2012) also sorted their bulk data (brown squares; see their Fig. 6(a)) into two groups according to the wave conditions: no/following/opposing swell (green dashed line) and cross swell (red dashed line) (see their Table 2). The reader is referred to the legend and reference therein for all the details. (For interpretation of the references to colour in this figure legend, the reader is referred to the web version of this article.)

verse accuracy of each model in estimating H_s under Ivan, it is necessary to carefully examine and inter-compare C_d from all the five wave models. Fig. 9 presents C_d estimated by the five models as a function of U_{10r} (the wind speed U_{10} relative to the ocean surface current velocity (see Appendix of Edson et al., 2013))⁶, together with a number of published parameterizations and measurements from field and laboratory experiments (see the caption and legend of this figure). The model results are averaged into 2 ms^{-1} bins of U_{10r} and shown as solid lines. Values in between 5th and 95th percentiles of C_d for each 2- ms^{-1} bin are also illustrated by the shaded region. Furthermore, we only retain C_d values from deep sea points (depth is greater than 500 m) to preclude the strong nonlinearity of waves in the coastal environment, which is believed to increase C_d somewhat (e.g., Babanin and Makin, 2008).

Several interesting features can be identified from Fig. 9. Both ST2 (blue solid lines and shaded region) and ST3 (yellow solid lines and shaded region) have incorporated a sea state-dependent wind stress into their wind input source term S_{in} (Tolman and Chalikov, 1996; Janssen, 1991). Hence in low to moderate wind conditions ($U_{10} < 25 m s^{-1}$), C_d from these two models are not dependent on U_{10} only, as revealed by the corresponding envelopes. Same as ST3, ST4 also adopts the wind input function from Janssen (1991). Additionally introducing a sheltering effect by ST4, which reduces S_{in} at high frequencies by modifying wind stress u_* (Ardhuin et al., 2010), almost totally suppresses the dependence of C_d on sea state (green solid line). Similar results can also be found in Raschle and

Ardhuin (2013) (see their Fig. 12). ST6 implements a physical constraint that the wave supported norm stress ($\tau_w = \rho_w g \int \frac{S_m(f)}{c(f)} df$, where ρ_w is the density of sea water and g is gravity acceleration) cannot exceed the total wind stress ($\tau_{tot} = \rho_a C_d U_{10}^2$; ρ_a is the air density and Eq. (1) is selected to estimate C_d from U_{10}) less the viscous stress (Tsagareli et al., 2010). Therefore ST6-estimated C_d almost exactly follows Eq. (1) (red solid line in Fig. 9) without obvious deviation. C_d from UMWM show some sensitivity on other factors (e.g., sea state) besides the wind speed, as represented by the narrow gray envelope in Fig. 9. Such sensitivity is slightly more apparent when $U_{10} \in [30, 40] m s^{-1}$ (see also Fig. 21 of Donelan et al., 2012).

The changing trend of C_d with wind speed U_{10r} , as shown in Fig. 9, is an more important feature than their absolute values. It is known that the performance of numerical wave modelling is determined by the overall difference among source terms in RHS of Eq. (3). Uncertainty in one source term may be well cancelled by deficiencies in other terms. This is especially true when the wave breaking term S_{ds} is concerned, which so far remains as the least understood part and is known as a tuning knob in wave models (e.g., Cavaleri et al., 2007; Babanin et al., 2010). Therefore the slightly higher or lower C_d (and u_*) flowing into S_{in} might be compensated by the free parameters in S_{in} and S_{ds} through tuning exercises. According to Fig. 9 we know that all the three well-performed models, i.e., ST3/4/6, evidently exhibit the saturation or even decrease trend of C_d when U_{10r} approaches hurricane force ($33 m s^{-1}$). For ST2, it is apparent that the limit $C_{d,max} = 2.5 \times 10^{-3}$ is already activated when U_{10r} is far below the hurricane force. Undoubtedly the well tuned wind wave growth behaviour for low and moderate wind conditions as done in Tolman and Chalikov (1996) and Tolman (2002) should have been violated, which may explain the general underestimation of H_s by ST2 (Figs. 5

⁶ Using the method detailed in Donelan et al. (2012) (see their Section 2.3.2), UMWM calculates C_d for each sea point as a standard output parameter. By contrast, WW3 outputs wind stress u_* and its definition depends on selected source term parameterization (i.e., ST2/3/4/6). We simply converted WW3-outputs u_* by $C_d = u_*^2/U_{10r}^2$.

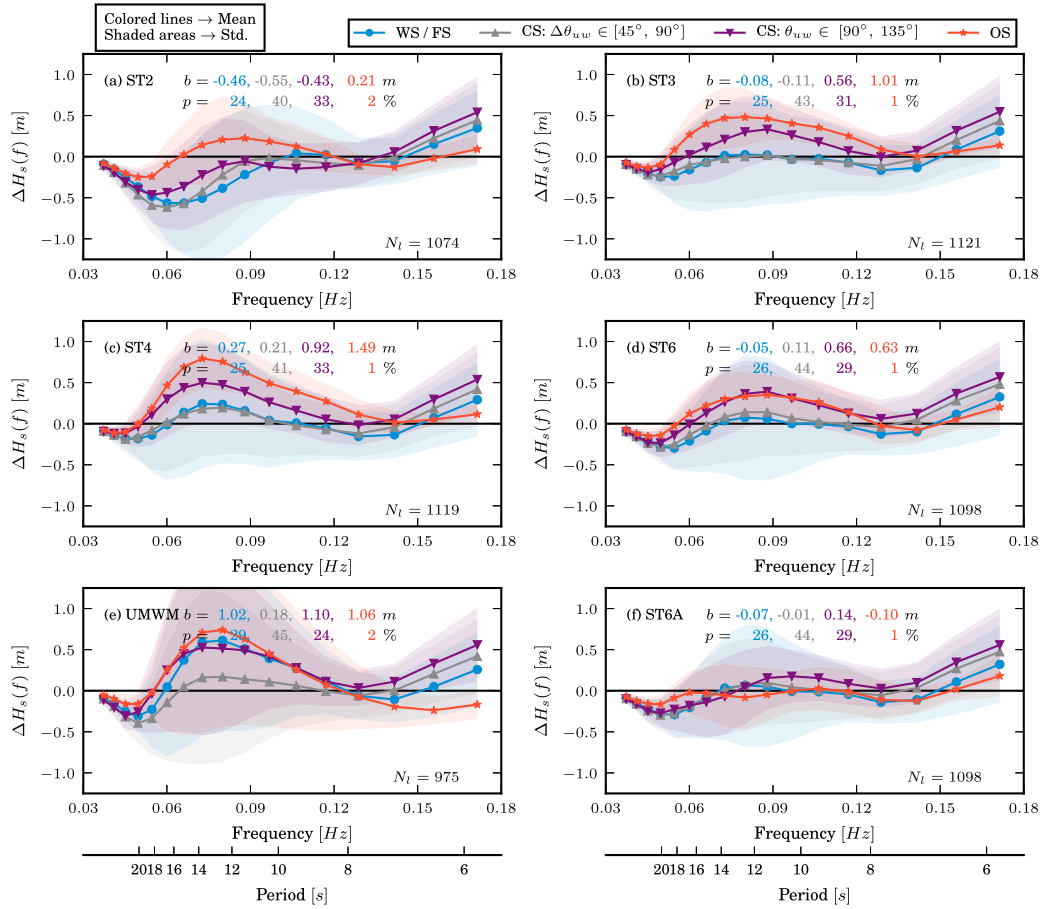


Fig. 10. Statistical comparison of 1D wave spectra $E(f)$ between SRA observations and model results from (a) ST2, (b) ST3, (c) ST4, (d) ST6, (e) UMWM and (f) ST6A ($a'_0 = 0.55$) (see Section 4.2 for explanations). Following Bidlot et al. (2007), the spectra data were smoothed by averaging over 3 consecutive wave model frequency bins and then were converted to equivalent wave heights, i.e., $H_s(f) = 4\sqrt{\int_{f_l}^{f_h} E(f)df}$, where f_l and f_h are the low and high boundaries of the frequency bin in question. For each frequency bin, the average (solid line with markers) and standard deviation (shaded area) of the differences ($\Delta H_s(f)$) between model results ($H_{s,i}^m(f)$) and SRA observations ($H_s^o(f)$) are shown. The model-SRA collocated pairs are sorted into four groups according to their swell regimes (see Fig. 2(d, e)): (blue) wind sea or following swell (WS / FS), (gray) cross swell (CS) with $\Delta\theta_{uw} \in [45^\circ, 90^\circ]$, (purple) CS with $\Delta\theta \in [90^\circ, 135^\circ]$ and (red) opposing swell (OS). Model results with high errors in θ_w (i.e., the relative angle between model-simulated and SRA-observed θ_w is greater than 25°) are excluded from this analysis. The total number of remaining collocations (N_i) is presented in the lower-right corner of each panel. Besides, the overall bias of H_s (b) for each group and the proportion each group accounts for (p) are also printed in the top part of each panel. (For interpretation of the references to colour in this figure legend, the reader is referred to the web version of this article.)

and 6). Different from other four models, UMWM provides increasing C_d with the increasing U_{10r} throughout the range of U_{10r} in which we are concerned ($2\text{--}60\text{ m s}^{-1}$), although the increasing rate relaxes somewhat when U_{10r} is beyond 33 m s^{-1} . Below 20 m s^{-1} , C_d from UMWM is close to the CBLAST-Hurricane field measurements (Black et al., 2007) and the parameterization suggested by Holthuijsen et al. (2012) for FS and OS conditions (Section 2.1.3). Above 30 m s^{-1} , UMWM-computed C_d approximates to the laboratory measurements from Donelan et al. (2004). The slope of UMWM-estimated C_d is lower than those for the four other models under low and moderate wind conditions ($U_{10r} < 20\text{ m s}^{-1}$), which follow more closely the parameterizations formulated by Wu (1982) and Edson et al. (2013) (i.e., COARE 3.5 algorithm). Under high wind regime ($U_{10r} > 30\text{ m s}^{-1}$), the situation is reversed. Such inconsistency might be responsible for the drawback of UMWM we saw in the previous section, i.e., underestimation of low H_s and overestimation of high H_s .

4.2. Negative wind input

In Fig. 10, we present statistical comparisons of 1D wave spectra $E(f)$ between SRA observations and model results. Following

Bidlot et al. (2007), the spectra data were smoothed by averaging over 3 consecutive wave model frequency bins and then were converted to equivalent wave heights, i.e., $H_s(f) = 4\sqrt{\int_{f_l}^{f_h} E(f)df}$, where f_l and f_h are the low and high boundaries of the frequency bin in question. The average and standard deviation of $\Delta H_s(f) = H_s^m(f) - H_s^o(f)$ (the superscript m and o identify model results and SRA observations) for each frequency bin are shown as solid lines (with markers) and shaded regions, respectively. As in Fig. 2(d, e), we categorized model-SRA pairs into four groups according to the SRA-observed wave conditions: WS/FS, CS with $\Delta\theta_{uw} \in [45^\circ, 90^\circ]$ (hereafter CSP, where “P” identifies positive $\cos \Delta\theta_{uw}$), CS with $\Delta\theta_{uw} \in [90^\circ, 135^\circ]$ (hereafter CSN; “N” for negative $\cos \Delta\theta_{uw}$) and OS. Such classification approach requires that wind direction θ_u should be accurate enough. Unrealistic wind directions tends to cause wave model to yield unreasonable wave directions. Given this, we excluded the model-SRA pairs from the analysis when model errors in θ_w is greater than 25° (around the RMSE ε of model-estimated θ_w ; see Table 2). In this way, the two special flight segments from September 09, i.e., Point 60-100 and Point 250-300 as we mentioned earlier, are basically filtered out from the following analysis. Careful examination of our results proved

that such filtering did not result in obvious deviations from what we presented in Fig. 10.

The three well-performing models, i.e., ST3/4/6, as identified in Section 3, share some similarities in estimating H_s (Fig. 10 (b–d)). On average, sea states prevalent in the right (strong) side of the hurricane track, i.e., WS/FS (blue line with dots; accounting for ~25% of the records we retained) and CSP (gray line with upward triangles; accounting for ~40%), are relatively well-predicted by the three models; whereas CSN (purple line with downward triangles; accounting for ~30%) and OS (red line with stars; accounting for ~1%), common in the left (weak) side of the hurricane track, are more apparently overestimated in varying degrees. For instance, ST6 gives biases of 0.66 m and 0.63 m for CSN and OS, which are more than 0.5 m higher than those for WS/FS and CSP (–0.05 m and 0.11 m, respectively). Consequently, the H_s estimated by ST6 is around 1 m more biased in the left side than in the right side of the hurricane track ($b = 0.80$ m vs. $b = -0.12$ m; not shown). ST2 and UMWM (Fig. 10 (a, e)) are also inclined to overestimate H_s of OS. For other types of sea states, however, they behave differently from ST3/4/6. Considering the deficiencies of ST2 and UMWM we discussed in previous sections, such behaviours are not unexpected. Here we concentrate on ST3/4/6 models only and scrutinize the problem we just posed: why was H_s of WS/FS and CSP generally well-estimated but in the meantime CSN and OS were clearly over-predicted by models?

One possible candidate responsible for the overestimation of H_s of CSN and OS may be that the attenuation of swell due to the oblique and adverse winds in ST3/4/6 is not strong enough. The wind-induced swell decay – sometimes also termed as the negative wind input into swell (related to S_{swl} in Eq. (3)), has been implemented differently in ST3/4/6. In the following discussions, we will select ST6 only to illustrate such effect on simulations of CSN and OS.

Laboratory and field experiments have revealed that swell outrunning or propagating against winds will transfer momentum flux from waves to the winds and therefore dissipation of the swell waves (e.g., Donelan, 1999; Kahma et al., 2016). The attenuation rate of swell in such cases, however, is not clearly defined yet. Typically, the wind-induced wave growth/attenuation rate γ is defined as follows (e.g., Donelan et al., 2006):

$$\gamma(f) = \frac{\rho_w}{\rho_a} \frac{1}{\sigma E(\sigma)} \left. \frac{\partial E(\sigma)}{\partial t} \right|_{\text{wind}}, \quad (5)$$

where $E(\sigma) = E(f)/2\pi$ is the 1D radian-frequency spectrum. The benchmarking experiment conducted in the laboratory by Donelan (1999) yields

$$\gamma(f) = s(U_{\lambda/2}/c(f) - 1)|U_{\lambda/2}/c(f) - 1|, \quad (6)$$

$$s = \begin{cases} 0.28 & \text{for } U_{\lambda/2}/c(f) - 1 \geq 0 \\ 0.11 & \text{for } U_{\lambda/2}/c(f) - 1 < 0 \end{cases} \quad (7)$$

where $U_{\lambda/2}$ is the wind speed at the height of one-half of the wavelength λ , c is the phase speed, s is the so-called sheltering coefficient. It should be noted that the sheltering coefficient s of 0.11 for $U_{\lambda/2}/c - 1 < 0$ was only estimated from cases where swells were travelling exactly in adverse winds, i.e., OS. According to Eq. (7), the attenuation rate of OS corresponds to a sheltering coefficient about 0.4 times that for the growth rate of WS. In Donelan et al. (2012), the authors proposed another set of sheltering coefficients for γ through model tuning exercises with UMWM:

$$\gamma(f, \theta) = s(U_{\lambda/2} \cos \theta' / c(f) - 1)|U_{\lambda/2} \cos \theta' / c(f) - 1|, \quad (8)$$

Table 3

Inter-comparison of five studies on wind-induced swell attenuation. All the reported sheltering coefficients were converted to equivalent a_0 as in Zieger et al. (2015). Following Donelan et al. (2012), we sorted the values into two groups according to the wave characteristics: $0 < U_s \cos \theta' / c(f) < 1$ (long FS and CSP) and $\cos \theta' < 0$ (OS and CSN). U_s is the representative scaling wind speed and “n/a” means equivalent a_0 was not available for the particular group from the given study. It should be noted that a_0 for Reichl et al. (2014), labelled with †, were only approximating values estimated from their Eq.(14).

	$0 < U_s \cos \theta' / c(f) < 1$	$\cos \theta' < 0$
Donelan (1999)	n/a	$a'_0 = 0.11/0.28 = 0.40$
Donelan et al. (2012)	$a_0 = 0.01/0.11 = 0.09$	$a'_0 = 0.10/0.11 = 0.91$
Reichl et al. (2014)	$a_0 \approx 5/25 = 0.20^\dagger$	$a'_0 \approx 25/25 = 1.00^\dagger$
Zieger et al. (2015)	$a_0 = 0.09$	$a'_0 = 0.09$
Kahma et al. (2016)	$a_0 = 0.03/0.21 = 0.14$	n/a

$$s = \begin{cases} 0.11 & \text{for } U_{\lambda/2} \cos \theta' \geq c(f) \\ 0.01 & \text{for } 0 < U_{\lambda/2} \cos \theta' < c(f), \\ 0.10 & \text{for } \cos \theta' < 0 \end{cases}, \quad (9)$$

where θ' is the angle between wind (θ_u) and waves of frequency f and direction θ . Based on Eq. (9), we know that in UMWM the s for the attenuation rate of CSN and OS ($\cos \theta' < 0$) is as high as 0.91 times that for the growth rate of WS ($U_{\lambda/2} \cos \theta' \geq c(f)$). Such high swell decay rate has been closely followed by Reichl et al. (2014) to calculate wind stress under hurricane winds. Following Donelan (1999), Zieger et al. (2015) also parameterized the wind-induced decay of swell into S_{in} of ST6 by

$$\gamma(f, \theta) = \begin{cases} \mathcal{F}(|U_s \cos \theta' / c(f) - 1|) & \text{for } U_s \cos \theta' / c(f) - 1 \geq 0 \\ -a_0 \mathcal{F}(|U_s \cos \theta' / c(f) - 1|) & \text{for } U_s \cos \theta' / c(f) - 1 < 0 \end{cases} \quad (10)$$

where \mathcal{F} represents a function of wave slope and degree of flow separation as described in Donelan et al. (2006) and Babanin et al. (2007), U_s is the scaling wind speed ($\sim 28u_*$), a_0 is a tuning parameter that controls the strength of swell decay due to wind effects. It essentially signifies the ratio of s for wind-induced swell decay to that for wind wave growth. Zieger et al. (2015) found $a_0 = 0.09$ fitted the bulk altimeter data reasonably in their global hindcast experiments and consequently adopted such value as the default setting of ST6. Unlike Donelan et al. (2012), Zieger et al. (2015) did not distinguish long FS and CSP (i.e., $0 < U_r \cos \theta' < c(f)$) from OS and CSN (i.e., $\cos \theta' < 0$).

Recently, Kahma et al. (2016) reanalyzed the measurements from one field experiment they undertook in Lake Ontario some thirty years ago in 1987, and reported their results can be approximately fitted by:

$$\gamma(f) = s(U_{12}/c(f) - 1)|U_{12}/c(f) - 1|, \quad (11)$$

$$s = \begin{cases} 0.21 & \text{for } U_{12}/c(f) - 1 \geq 0 \\ 0.03 & \text{for } U_{12}/c(f) - 1 < 0 \end{cases}. \quad (12)$$

In Eq. (12), U_{12} is the wind speed at 12 m height and only long FS was selected to compute s for $U_{12}/c(f) - 1 < 0$.

The five aforementioned studies, including Reichl et al. (2014), actually can be inter-compared through simply converting the corresponding s into an equivalent a_0 (Eq.(10)) for different wave conditions, as presented in Table 3. For differentiation, values of a_0 for cases where $\cos \theta' < 0$ (CSN and OS) is denoted as a'_0 in Table 3 and hereafter. It is notable that for swell outrunning the winds ($0 < U_s \cos \theta' / c(f) < 1$; long FS and CSP), a_0 from all the five studies vary in a narrow range from 0.09 to 0.20, centering around

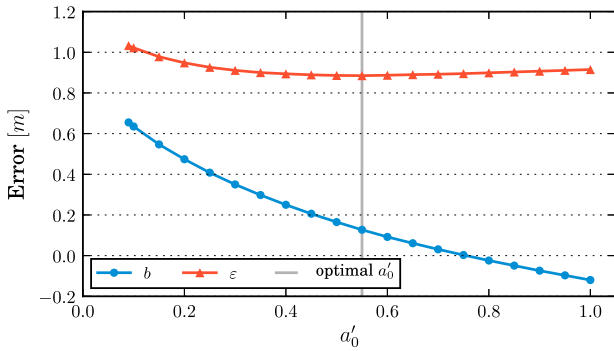


Fig. 11. Errors of ST6-simulated H_s of CSN and OS as a function of a'_0 : (blue) bias b and (red) RMSE ε . The gray solid line highlights at where ε is minimized. (For interpretation of the references to colour in this figure legend, the reader is referred to the web version of this article.)

the observed-value (0.14) from Kahma et al. (2016). On the contrary, a'_0 for swell travelling against winds ($\cos\theta' < 0$; CSN and OS) is quite scattered. The ST6-favored a'_0 (0.09) is apparently smaller than others. As mentioned earlier, Zieger et al. (2015) tuned a'_0 (same as a_0) from hindcasts of waves in the global basin, where statistically CSN and OS may be not as frequently occurred as under hurricane conditions. Thus such special situations are possibly not well represented by the tuning exercises completed on the bulk of the data (Cavaleri, 2009). As will be shown later, properly enhancing a'_0 of ST6 in opposing winds (i.e., $\cos\theta' < 0$) can effectively solve the overestimation of CSN and OS. This is achieved through modifying Eq. (10) as follows:

$$\gamma(f, \theta) = \begin{cases} \mathcal{F}(|U_r \cos\theta'/c(f) - 1|) & \text{for } U_r \cos\theta'/c(f) - 1 \geq 0 \\ -a_0 \mathcal{F}(|U_r \cos\theta'/c(f) - 1|) & \text{for } 0 < U_r \cos\theta' < c(f) \\ -a'_0 \mathcal{F}(|U_r \cos\theta'/c(f) - 1|) & \text{for } \cos\theta' < 0 \end{cases}, \quad (13)$$

where $a_0 = 0.09$ is left unchanged as FS and CSP are generally well-predicted by ST6.

Fig. 11 presents the errors of ST6-estimated H_s of CSN and OS as a function of a'_0 , starting from the default value of ST6 (0.09) and ending at 1.00 as adopted in Reichl et al. (2014). Unsurprisingly, the bias b (blue line with dots) decreases monotonically with increasing a'_0 . By contrast, the RMSE ε (red line with triangles) shows its minimum at $a'_0 = 0.55$ (highlighted by the gray solid line in Fig. 11). Interestingly, the optimal a'_0 (0.55) obtained here does not deviate too much from the observed value (0.4) from Donelan (1999), particularly when compared with Donelan et al. (2012) and Reichl et al. (2014) (see a further discussion on the value of a'_0 in Section 4.3). Examination of Fig. 10 (f) demonstrates that using $a'_0 = 0.55$ (denoted as ST6A in that panel and hereafter) notably improves the model skill in predicting H_s of CSN and OS at frequencies below ~ 0.13 Hz (wave periods greater than ~ 8 s). The frequency-dependent errors $\Delta H_s(f)$ for CSN and OS now does not differ too much from those for WS/FS/CSP (see Fig. 10 (d) for comparison). It also should be noted that wave components at frequencies beyond 0.13 Hz tend to well align with wind direction and therefore are not affected by negative S_{in} .

Fig. 12 illustrates the impacts of enhancing negative S_{in} on wave spectral details. For brevity, only two cases are presented: (a–c) for $\theta_{uw} \approx 100^\circ$ and (d–f) for $\theta_{uw} \approx 130^\circ$. In the first case, the observed spectrum shows a distinct peak at about 0.07 Hz and a gradual transition towards wind direction with increasing frequency. The ST6-simulated $F(f, \theta)$ (Fig. 12(b)) closely follows such spectral structure except the wave peak is too strong. Such overestimation can be considerably reduced by ST6A (Fig. 12(c)). Note that ST6-modeled spectra possess a broader wind sea tail, both in fre-

quency and directional domains, than SRA measurement (Fig. 12(b, c) vs. (a)). This is a common feature among our results and thus explains the overestimation of wave height at higher frequencies (beyond 0.13 Hz; Fig. 10). We should also bear in mind that DIA is known for broadening the directional and frequency spectra, as discussed in Zieger et al. (2015) for example (see their Fig. 7). In the second case, the observed spectrum (Fig. 12 (d)) shows two well-separated partitions: one swell system peaked at ~ 0.07 Hz and another wind sea system peaked at ~ 0.14 Hz. Whereas, the modeled spectra (Fig. 12 (e, f)) still show a similar feature as in previous case (Fig. 12 (b, c)) with the secondary wind sea peak being totally absent. Nonetheless, ST6A is still helpful to lower the modeled stronger swell peak (Fig. 12 (f)).

We note that the special situation where wind sea peak is missing in the model result, as we presented in Fig. 12 (d), has been discussed in Fan and Rogers (2016) (see the bottom panels of their Fig. 5; the authors used ST4 in their simulations). They speculated that the overestimation of swell and underestimation of wind sea in such situations are possibly because: (i) the driving wind data from H*Wind system is too smooth to characterize the fine structure of Ivan; (ii) the source functions S_{in} and S_{ds} , which were developed under low to moderated wind speeds, may be not applicable in challenging hurricane regime conditions. Here we comment another possibility that the directional distribution of S_{ds} also plays a role in the evolution of such complex spectra. In the contemporary wave models, the directional distribution of wave breaking-induced dissipation rate $\gamma_{ds}(f, \theta) (\propto S_{ds}/F(f, \theta))$, is typically implemented as isotropic. Young and Babanin (2006) found experimentally that γ_{ds} may be higher at oblique angles than that in the main wave propagation direction (wind direction in their context). Therefore, the widely used isotropic γ_{ds} may dissipate wave components travelling in the wind direction too much, resulting in the missing of the secondary wind sea peak in Fig. 12 (d–f). The effects of directional spreading of S_{ds} on wave simulations, however, is beyond the scope of this paper and is left for future research.

4.3. Nonlinear wave-wave interaction

Limited by its approximating nature, the DIA algorithm for S_{nl} has some well-known shortcomings (e.g., Cavaleri et al., 2007; Resio and Perrie, 2008; Perrie et al., 2013; Tolman, 2013; Rogers and Van Vledder, 2013). Tolman (2013) found that DIA can give rise to systematic errors of as high as 20% in H_s under hurricane conditions – specifically, over(under)-estimation of H_s in the left (right) side of hurricane tracks (see his Fig. 8 and Figs. 5.2 and 5.3 of Tolman, 2010). This indicates that DIA may also, at least partially, result in overestimation of CSN and OS.

To investigate the impacts of DIA on our results, we conducted another experiment, in which a combination of ST6 physics and the exact solution for S_{nl} , i.e., Webb–Resio–Tracy (WRT) algorithm (Webb, 1978; Tracy and Resio, 1982; Resio and Perrie, 1991; van Vledder, 2006) was used (hereafter ST6W). Limited by the computational resources, we only run this model set up in the sub-region of our full domain (the region in the black box in Fig. 1) and compared the model results against the first set of SRA observations. The differences between ST6W and ST6 (purple dashed lines vs red solid lines in Fig. 5 (a–c)) mainly come from two particular flight segments, Point 60–100 and Point 250–300 (from the left-rear and right-rear quadrant as in Fig. 2 (a), respectively), where the directions of the driven wind forcing may be questionable (see Section 3.1). Despite this, we can see that with the same wind forcing, DIA can result in $\sim 20\%$ errors in H_s , similar to the findings in Tolman (2013). Fig. 13 presents the model errors in H_s of CSN as a function of frequency. As expected, WRT (green line) is helpful to lower the overestimated wave energy by DIA (blue line) at low frequencies, particularly for $f \leq 0.08$ Hz. It also lifts wave heights

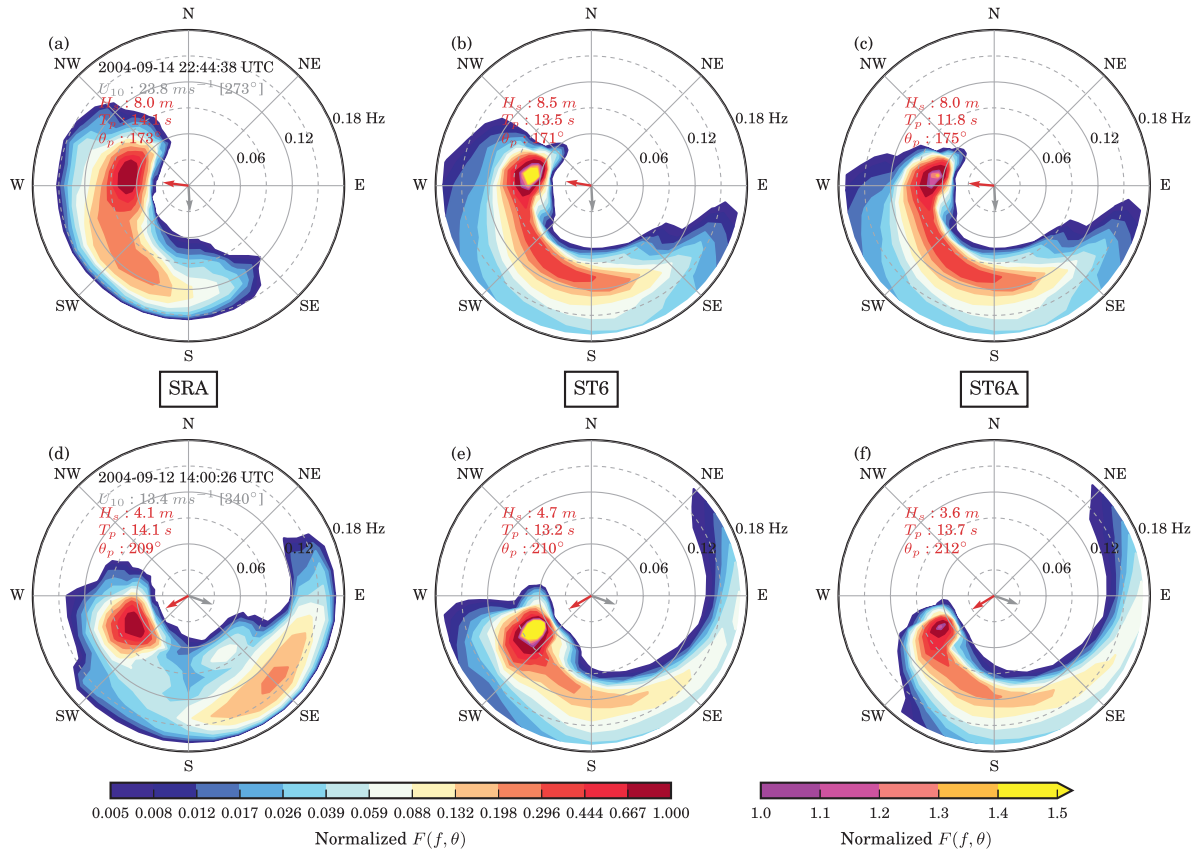


Fig. 12. Comparison of 2D wave spectrum $F(f, \theta)$ between (a, d) SRA observations and model results from (b, e) ST6 and (c, f) ST6A (i.e., ST6 with $a'_0 = 0.55$). Two cases are illustrated: (a–c) $\theta_{uw} \approx 100^\circ$ (Point 209 from the third set of SRA data; see Fig. 2 (c)) and (d–f) $\theta_{uw} \approx 130^\circ$ (Point 303 from the second set; see Fig. 2 (b)). The corresponding time and U_{10} (magnitude and direction) are shown together with SRA observations (panel (a, d)). Three integral wave parameters (wave height H_s , peak wave period and direction (T_p), estimated from $E(f)$ using a parabolic fit around the discrete peak, and $\theta_p = \arctan(\int \int F^4(f, \theta) \sin \theta d f d \theta / \int \int F^4(f, \theta) \cos \theta d f d \theta)$, as defined in Eq. (14) in Young, 2006)) are also presented in each panel. The gray and red arrows identify the direction of wind and peak waves (the Cartesian convention), respectively. For comparison, wave spectra have been normalized by the peak value of corresponding SRA spectrum. (For interpretation of the references to colour in this figure legend, the reader is referred to the web version of this article.)

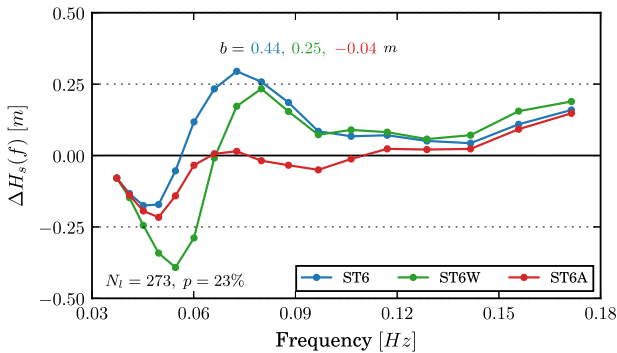


Fig. 13. Errors in H_s of CSN as a function of frequency ($\Delta H_s(f)$) for results from (blue) ST6, (green) ST6W and (red) ST6A. Data was processed in the same way as in Fig. 10 and only model results with sufficient accuracy in θ_w were kept. For the first set of SRA observations, 273 (N_i) spectra passed such filtering, among which CSN accounts for 23% (p). Only 3 OS spectra were obtained in this way and therefore were not presented in the analysis here for statistical significance. The overall biases in H_s of CSN provided by the three different models are printed in the top part of this figure. (For interpretation of the references to colour in this figure legend, the reader is referred to the web version of this article.)

slightly at frequencies beyond 0.13 Hz. The overall bias in H_s of CSN is decreased by WRT from 0.44 m to 0.25 m. Nonetheless, it should be highlighted that ST6A (red line) is more effective than ST6W in specifying H_s of CSN, as revealed by both the frequency-dependent errors ($\Delta H_s(f)$) and overall bias ($b = -0.04$ m). This jus-

tifies our efforts with the negative S_{in} in the previous subsection. The optimal value of $a'_0 = 0.55$ which were obtained with DIA, however, should be viewed with caution as it must have been affected somewhat by the shortcomings of DIA. It is also noteworthy that our simulations have some uncertainties, viz. DIA induced errors in S_{nl} , gust-factor tuned and rather smooth wind forcing, and assumed formulations for S_{ds} , etc. Accordingly, one should not attribute enhancing negative S_{in} as the only way to make all the model improvements.

In Section 2.2, we mentioned that UMWM parameterizes S_{nl} in a very distinct way which assumes wave breaking as the first-order mechanism that induces the downshifting of wave energy (Donelan et al., 2012). It is very interesting to understand how S_{nl} from UMWM quantitatively differs from DIA and WRT. As the last effort of this paper, we inter-compared these three different methods addressing S_{nl} , and present our results in Fig. 14. For comparison purposes, we switched other source terms (e.g., $S_{in} (+S_{swl}) + S_{ds}$) off and used parametric directional spectra for doing some academic tests only.

Three idealistic wave spectra were constructed by using the parametric spectral model for hurricane wind waves described in Young (2006) (see Appendix B). The first spectrum (Fig. 14 (a)) corresponds to a situation where the angle between wind and peak waves ($\Delta\theta_{uw}$) is around 25° (FS) and the other two are for situations where $\Delta\theta_{uw} \approx 90^\circ$ (CS; Fig. 14 (f)) and $\Delta\theta_{uw} \approx 160^\circ$ (OS; Fig. 14 (k)). For all the three cases, $U_{10} = 20 \text{ m s}^{-1}$ and $f_p = 0.1 \text{ Hz}$ were assumed, resulting in a peak enhancement factor γ of 2.3

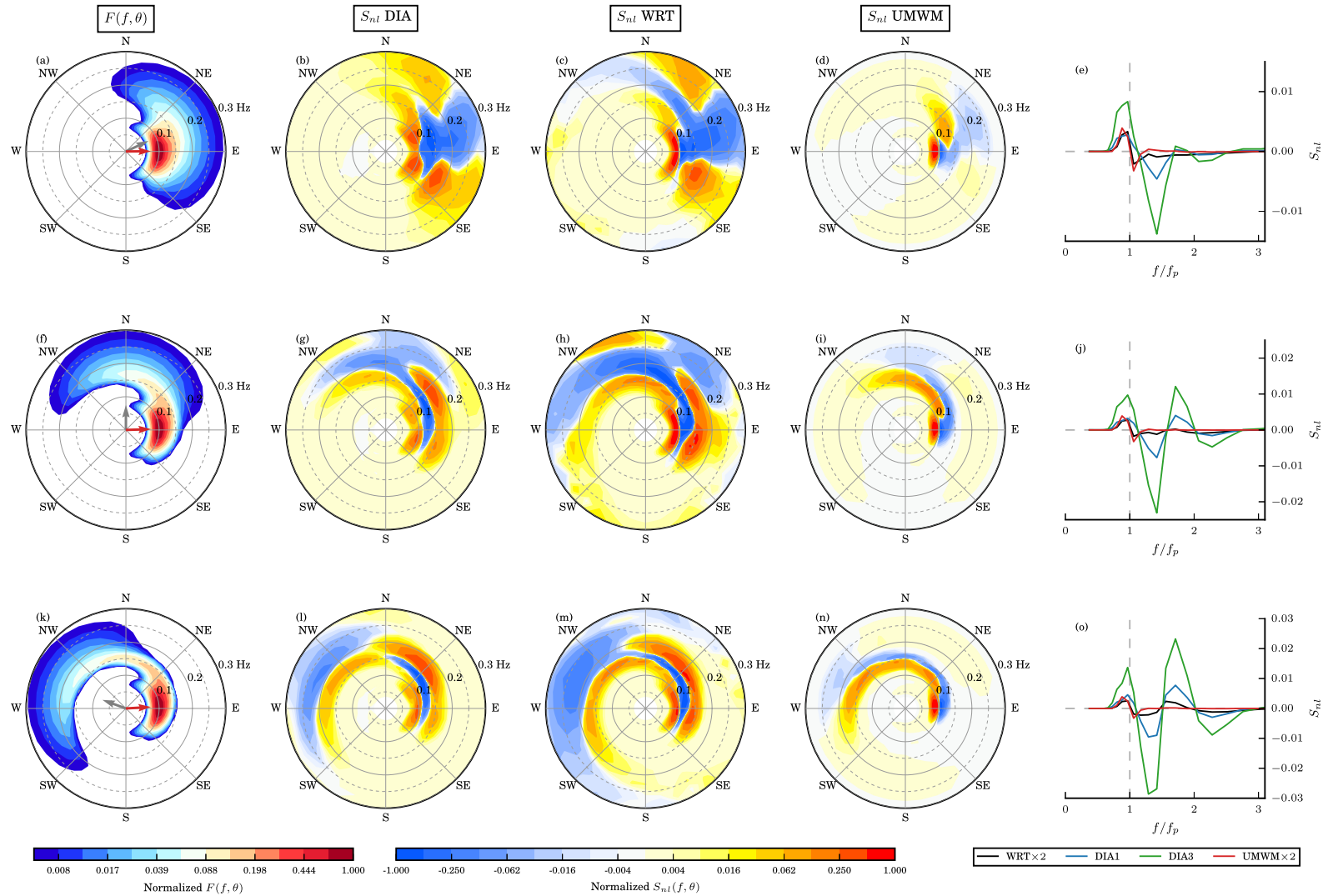


Fig. 14. Comparison of three different methods addressing S_{nl} . The panels to the extreme left illustrate the 2D wave spectra $F(f, \theta)$ for three cases: (a) $\Delta\theta_{uw} \approx 25^\circ$, (f) $\Delta\theta_{uw} \approx 90^\circ$ and (k) $\Delta\theta_{uw} \approx 160^\circ$. The red and gray arrows denote peak wave direction θ_p and wind direction θ_u , respectively. The parametric form detailed in Young (2006) (see Appendix B) was used to construct these three wave spectra ($H_s = 5.3$ m, $\gamma = 2.3$), for which $U_{10} = 20$ m s $^{-1}$, $f_p = 0.1$ Hz and $\theta_p = 0^\circ$ were assumed. Panels in the second, third and fourth columns present S_{nl} estimated by DIA, WRT and UMWM, respectively. To the extreme right, the 1D S_{nl} ($= \int S_{nl}(f, \theta) d\theta$) are shown as a function of non-dimensional frequencies (f/f_p): (black) WRT, (blue) DIA with $C = 1.0 \times 10^7$ as used by ST2 (DIA1 in the legend), (green) DIA with $C = 3.0 \times 10^7$ as used by ST6 (DIA3 in the legend) and (red) UMWM. Note that results given by WRT and UMWM were multiplied by a factor of 2 in panels (e, j, o) for clarity. All the 2D $F(f, \theta)$ and $S_{nl}(f, \theta)$ have been normalized by their corresponding maximal absolute value. (For interpretation of the references to colour in this figure legend, the reader is referred to the web version of this article.)

according to Eq. (B.4) and H_s of 5.3 m. The results for $S_{nl}(f, \theta)$ from DIA, WRT and UMWM are illustrated in the second, third and fourth columns of Fig. 14, respectively. In addition, the 1D S_{nl} , as a function of non-dimensional frequency (f/f_p), is also summarized in the extreme right column of Fig. 14.

The $S_{nl}(f, \theta)$ patterns from DIA are generally consistent with those from WRT, at least at the first order. Whereas, the magnitude of DIA results (the default setting with $C = 3.0 \times 10^7$ as in Hasselmann et al., 1985; DIA3 in the legend of our Fig. 14) are several times higher than WRT, as reflected by the 1D S_{nl} presented in Fig. 14 (e, j, o). Such quantitative disagreement between DIA and WRT is not unexpected and is consistent with results reported in Resio and Perrie (2008) and Perrie et al. (2013). On the contrary, S_{nl} estimated by UMWM is on the same magnitude as WRT results. The UMWM-estimated $S_{nl}(f, \theta)$ patterns, however, deviate notably from WRT. The positive lobe of S_{nl} from WRT at frequencies below f_p can be basically well-matched by UMWM, especially for 1D results. But the negative lobe given by UMWM at frequencies slightly above f_p is too narrow. Besides, for the CS and OS cases (Fig. 14 (f, k)), UMWM is not able to yield the secondary positive and negative lobes given by WRT and DIA at $\sim 1.7f_p$ and $\sim 2.3f_p$. This drawback existing in S_{nl} term of UMWM should be another important factor that causes UMWM to deviate from WW3-type models (Section 3).

5. Concluding remarks

Taking a well-observed hurricane case Ivan (2004) as an example, we investigated and inter-compared the performance of different wave models – UMWM and four source term packages from WW3 (ST2/3/4/6) – under hurricane conditions. The main findings can be summarized as follows:

- 1) The analysis of the SRA-observed 1432 wave spectra suggests in the vicinity of hurricane center, sea states in the right-front, left-front and rear sectors are generally dominated by FS, CS and OS, respectively. In the farther afield, although FS and OS can still be identified, CS occurs most frequently. Such results are generally consistent with the findings reported by Hu and Chen (2011) and Holthuijsen et al. (2012). Another feature supported by our data is that CSN (CS with $\Delta\theta_{uw} \in [90^\circ, 135^\circ]$) mainly appears in the left (weak) side of the hurricane track, as contrasted with CSP (CS with $\Delta\theta_{uw} \in [45^\circ, 90^\circ]$) which is primarily present in the right (strong) side.
- 2) A dynamic (model-dependent) gust factor (G_f^m) was utilized to optimize the wind forcing from H*Wind system. Once G_f^m was applied, each wave model we concern could basically give reasonable estimations of bulk wave parameters (i.e., H_s , θ_w , T_{02}). From the statistics summarized in Table 2 and the comparisons illustrated in Figs. 5–8, we know that ST3/4/6 relatively outperform ST2 and UMWM. Specifically, ST2 tends to underestimate wave periods and high waves ($H_s > 6$ m); whereas UMWM is inclined to underestimate H_s lower than 5 m and over-specify H_s greater than 10 m.
- 3) The upper limiter on C_d adopted by ST2 ($C_{d,max} = 2.5 \times 10^{-3}$) starts being active when U_{10} is far below the hurricane wind forcing ($U_{10} \sim 15$ m s $^{-1}$), which will influence the well-tuned wind wave growth behaviour under low to moderate winds (Tolman and Chalikov, 1996) and therefore may explain the underestimation of high waves by ST2.
- 4) The slope of UMWM-estimated C_d is relatively lower for low and moderate winds ($U_{10} \leq 20$ m s $^{-1}$). Besides, C_d from UMWM does not saturate at hurricane forcing, that is, it increases continuously with increasing U_{10} throughout the range of U_{10} in which we are concerned ($[2, 60]$ m s $^{-1}$). Such changing trend of C_d may in some degree explain its underestimation of small waves and overestimation of high waves. We also find that the

S_{nl} term of UMWM deviates notably from WRT solution in the spectral patterns. Particularly for CS and OS cases, UMWM is not capable to yield the secondary positive and negative lobes at frequencies beyond f_p .

- 5) For the three well-performed wave models (ST3/4/6), a common feature of model error is that H_s of CSN and OS is apparently overestimated in varying degrees. With ST6, we showed that enhancing negative S_{in} appropriately can effectively solve such problem (Fig. 10 (d, f) and Fig. 12 (a–c)). The optimal value of a'_0 (0.55), one parameter controlling the strength of wind induced swell decay for CSN and OS cases in S_{in} of ST6, does not deviate too much from the observed value (0.4) as reported in Donelan (1999), particularly when compared against values derived from Donelan et al. (2012) and Reichl et al. (2014).

It should be aware that there are some limitations in our study. First, this is only a case study for Ivan (2004). To generalize the findings presented above, a large sample of hurricanes (and extratropical storms) should be collected, simulated and analyzed. This is especially true and necessary for the operational weather/wave forecasting purpose (e.g., Chao and Tolman, 2010). Second, The H*Wind data are known as too smooth to characterize the fine structure of hurricanes. The intensity and structure changes during hurricane eyewall replacement cycles are totally missing in the H*Wind data by design (e.g., Terwey and Montgomery, 2008; Sitkowski et al., 2011). This may also partly explain the less accuracy of modelled wave direction θ_w , compared against that of H_s and T_{02} (our Fig. 5, see also The WAMDI Group, 1988, p. 1794). Hence we should bear in mind that the errors in wind forcing (and similarly ocean currents) should not be ignored and the assumption that the wind error is smaller than physics errors from wave models may be questionable.

Nonetheless, having stated the limitations and findings of the present study, we think it might be useful to pursue the following for future research to improve the performance of wave models under severe weather conditions:

- 1) incorporating the measured directional behavior of wave-breaking dissipation rate γ_{ds} (Young and Babanin, 2006) into S_{ds} , which are higher at oblique angles than in the peak wave direction, and test such effect on the simulated wave spectra;
- 2) replacing DIA with the Generalized Multiple DIA (GMD) algorithm recently developed by Tolman (2013), which was proved capable of removing most of the errors of DIA at only 2–3 times more costs (see Table 4 of Tolman, 2013). A preliminary test of ST2 with GMD (Appendix C) does show improvements over ST2+DIA run, particularly for wave period T_{02} (ε was reduced by 14–20%), indicating the rather dramatic changes in spectral shape introduced by the GMD approach. It is therefore necessary to optimize GMD for other source term packages (i.e., ST3/4/6) and most importantly to consider how to optimize the tuning parameters of GMD and $S_{in} (+S_{swl}) + S_{ds}$ independently (Tolman and Grumbine, 2013).

Acknowledgment

The authors are grateful to Dr. Dave Duncalf and Dr. Simon Caine from Offshore Weather Service, Melbourne, Australia, and Dr. Jian-Guo Li from Met office, United Kingdom for extensive discussion. We appreciate Prof. James B. Edson from University of Connecticut for providing his codes on the COARE3.5 algorithm. We also acknowledge Dr. Milan Curcic from University of Miami for his help on running UMWM. Q. Liu acknowledges the support from China Scholarship Council (CSC; 201406330003) and the DISI Australia-China Centre through grant ACSRF48199. AVB acknowledges support from the Australian Research Council Discovery Grant DP170100851 and the U.S. Office of Naval

Research Grant N00014-13-1-0278. C. Guan appreciates the financial support by Ministry of Science and Technology of China (No.2016YFC140140005). The authors are thankful for all comments and criticism raised by the editor and three independent reviewers which have improved our manuscript a lot.

Appendix A. Statistics for model validation

In our study, three bulk (integral) wave parameters, including significant wave height H_s , mean wave direction θ_w and mean wave period T_{02} , were selected to check the performance of different source term packages. Given a 2D frequency-directional spectrum $F(f, \theta)$, these three bulk parameters can be written as follows:

$$H_s = 4 \sqrt{\int_0^{2\pi} \int_0^{f_{\max}} F(f, \theta) df d\theta}, \quad (\text{A.1})$$

$$\theta_w = \arctan \left(\frac{\int_0^{2\pi} \int_0^{f_{\max}} F(f, \theta) \sin \theta df d\theta}{\int_0^{2\pi} \int_0^{f_{\max}} F(f, \theta) \cos \theta df d\theta} \right), \quad (\text{A.2})$$

$$T_{02} = \left(\frac{\int_0^{2\pi} \int_0^{f_{\max}} F(f, \theta) df d\theta}{\int_0^{2\pi} \int_0^{f_{\max}} f^2 F(f, \theta) df d\theta} \right)^{1/2}, \quad (\text{A.3})$$

where f_{\max} is the upper limit of frequencies. In the model-SRA (model-buoy) comparison, f_{\max} was chosen as 0.17 (0.485) Hz, limited by the highest resolved frequency by the SRA (buoys).

The four following statistical parameters: bias b , RMSE ε , correlation coefficient ρ and scatter index (SI), were utilized to quantify model skill:

$$b = \frac{1}{N} \sum_{i=1}^N (x_i - y_i), \quad (\text{A.4})$$

$$\varepsilon = \sqrt{\frac{1}{N} \sum_{i=1}^N (x_i - y_i)^2}, \quad (\text{A.5})$$

$$\rho = \frac{\sum_{i=1}^N (x_i - \bar{x})(y_i - \bar{y})}{\sqrt{\sum_{i=1}^N (x_i - \bar{x})^2 \sum_{i=1}^N (y_i - \bar{y})^2}}, \quad (\text{A.6})$$

$$SI = \frac{\sqrt{\frac{1}{N} \sum_{i=1}^N [(x_i - \bar{x}) - (y_i - \bar{y})]^2}}{\bar{y}}, \quad (\text{A.7})$$

where x and y represent the *simulated* and *measured* wave quantities, the bar over x and y denotes their mean value, and N is the sample size of the collocations. For the variable θ_w , only the RMSE ε is computed and the difference between two angles (in degree) are limited in $[0^\circ, 180^\circ]$.

Taylor diagram (Taylor, 2001) is a useful tool to summarize multiple error metrics in a single graph, providing a good way to illustrate how closely a pattern (simulation) matches observations. Apart from the correlation coefficient ρ defined above (Eq. (A.6)), a Taylor diagram can also present the normalized standard deviation σ_n and the normalized centered root-mean-square error ε_n^c :

$$\sigma_n = \frac{\sqrt{\sum_{i=1}^N (x_i - \bar{x})^2}}{\sqrt{\sum_{i=1}^N (y_i - \bar{y})^2}}, \quad (\text{A.8})$$

$$\varepsilon_n^c = \frac{\sqrt{\sum_{i=1}^N [(x_i - \bar{x}) - (y_i - \bar{y})]^2}}{\sqrt{\sum_{i=1}^N (y_i - \bar{y})^2}}. \quad (\text{A.9})$$

Appendix B. Directional spectra of hurricane wind waves

Based on an extensive buoy dataset, Young (2006) demonstrated the 1D and directional wave spectra of hurricane wind waves can be well-fitted by the parametric spectral form reported for uni-directional winds. Given the directional spectra $F(f, \theta)$ as follows:

$$F(f, \theta) = E(f)D(f, \theta), \quad (\text{B.1})$$

where $D(f, \theta)$ is a directional spreading function and satisfies the constraint that $\int D(f, \theta) d\theta = 1$. The 1D spectrum $E(f)$ can be represented by the parametric form proposed by Donelan et al. (1985), which reads

$$E(f) = \beta g^2 (2\pi)^{-4} f_p^{-1} f^{-4} \exp \left[- \left(\frac{f}{f_p} \right)^{-4} \right] \cdot \gamma \exp \left[\frac{-(f-f_p)^2}{2\sigma^2 f_p^2} \right], \quad (\text{B.2})$$

where β is a scale parameter, f_p is the peak frequency, c_p is the corresponding phase speed ($=g/2\pi f_p$ according to the linear dispersion relationship for deep water waves), γ is the peak enhancement factor and σ is the spectra width parameter. According to Young (2006), the functional dependence of β and γ on the inverse wave age (U_{10}/c_p) given by Donelan et al. (1985) is also applicable under hurricane regime and can be written as:

$$\beta = 0.006 (U_{10}/c_p)^{0.55}, \quad (\text{B.3})$$

$$\gamma = \begin{cases} 1.7 & \text{for } 0.83 < U_{10}/c_p < 1 \\ 1.7 + 6.0 \log_{10}(U_{10}/c_p) & \text{for } 1 < U_{10}/c_p < 5 \end{cases}. \quad (\text{B.4})$$

Whereas, σ estimated from buoy data is quite scattered and can be represented by the mean value of 0.11.

The directional spreading function $D(f, \theta)$ can be parameterized by the $\cos^{2s}\theta/2$ model (e.g., Mitsuyasu et al., 1975) (see also Young, 1999 ch. 5 and Holthuijsen, 2007 ch. 6):

$$D(f, \theta) = \frac{\Gamma(s+1)}{2\sqrt{\pi} \cdot \Gamma(s+\frac{1}{2})} \cos^{2s} \left(\frac{\theta - \theta_m(f)}{2} \right), \quad (\text{B.5})$$

where Γ is the gamma function, s is a parameter controlling the narrowness of distribution, $\theta_m(f)$ is the angle at which $D(f, \theta)$ is a maximum at frequency f . The buoy measurements in Young (2006) favor s depends on the non-dimensional frequency (f/f_p) in the following way:

$$s(f) = \begin{cases} 20 \left(\frac{f}{f_p} \right)^{4.5} & \text{for } f < f_p \\ 20 \left(\frac{f}{f_p} \right)^{-2.4} & \text{for } f \geq f_p \end{cases}. \quad (\text{B.6})$$

Regarding on $\theta_m(f)$, Young (2006) suggested that wave components below peak frequency f_p follow the peak wave direction for the full spectrum (i.e., θ_p) and the high frequency components beyond $2f_p - 3f_p$ are generally aligned with wind direction θ_u (see his Fig. 5). A smooth transition from θ_p to θ_u can be assumed for wave components at frequencies in between. In our simulations, we have closely followed such features and written $\theta_m(f)$ as below:

$$\theta_m(f) = \frac{\theta_u + \theta_p}{2} + \frac{\theta_u - \theta_p}{2} \cdot \tanh \left[4 \left(\frac{f}{f_p} - 1.5 \right) \right]. \quad (\text{B.7})$$

In Eq. (B.7), the condition $0^\circ \leq \theta_p < \theta_u < 360^\circ$ is assumed and the parameters 4 and 1.5 are arbitrarily chosen so that for $f \leq f_p$, $\theta_m(f) \approx \theta_p$ and for $f \geq 2f_p$, $\theta_m(f) \approx \theta_u$.

Table C.4Same as Table 2 but for the results of ST2 with different S_{nl} solvers (DIA and GMD).

Model	H*Wind U_{10} $G_f^m (b^H, \varepsilon^H)$	SRA								RA								
		$H_s [m]$				$\theta_w [^\circ]$				$T_{02} [s]$				$H_s [m]$				
		b	ε	ρ	SI	ε	b	ε	ρ	SI	b	ε	ρ	SI	b	ε	ρ	SI
ST2DIA	1.08 (0.00, 1.08)	-0.51	1.22	0.86	0.16	32.6	-0.49	0.85	0.68	0.07	-0.28	0.99	0.89	0.20				
ST2GMD	1.03 (0.02, 1.02)	-0.64	1.26	0.86	0.15	30.9	-0.28	0.73	0.72	0.07	-0.21	0.99	0.89	0.20				
Buoy																		
		$H_s [m]$								$T_{02} [s]$								
		b	ε	ρ	SI	b	ε	ρ	SI									
ST2DIA		-0.95	1.32	0.93	0.17	-0.87	1.20	0.75	0.10									
ST2GMD		0.91	1.28	0.94	0.17	-0.50	0.96	0.75	0.10									

Appendix C. Comparison between GMD and DIA

The GMD approach proposed by Tolman (2013) expands upon on DIA by generalizing the definition of the representative quadruplet and allowing for multiple representative quadruplets. Tolman (2013) showed that the G35 configuration of GMD method (five quadruplets and three-parameter quadruplet definition) is able to give nearly identical results to WRT but at much less cost. The tuning parameters of GMD, however, are heavily dependent on the source term package (i.e., $S_{in} + S_{ds} + S_{swl}$) that GMD is interacting with. Only configurations of GMD for ST2 were provided in Tolman (2013). We ran ST2 with the G35 configuration detailed in Table 2 of Tolman (2013) and found clear improvement over the ST2+DIA run in terms of wave period T_{02} (see Table C.4 for example).

References

Ardhuin, F., Chapron, B., Collard, F., 2009. Observation of swell dissipation across oceans. *Geophys. Res. Lett.* 36 (6), 1–5. doi:10.1029/2008GL037030.

Ardhuin, F., Rogers, E., Babanin, A., Filipot, J.-F., Magne, R., Roland, A., Van Der Westhuysen, A., Queffelec, P., Lefevre, J.-M., Aouf, L., Collard, F., 2010. Semi-empirical dissipation source functions for ocean waves: part I, definition, calibration and validation. *J. Phys. Oceanogr.* 40, 1917–1941. doi:10.1175/2010JPO4324.1.

Babanin, A.V., 2006. On a wave-induced turbulence and a wave-mixed upper ocean layer. *Geophys. Res. Lett.* 33 (20), L20605. doi:10.1029/2006GL027308.

Babanin, A.V., 2011. *Breaking and Dissipation of Ocean Surface Waves*. Cambridge University Press.

Babanin, A.V., Banner, M.L., Young, I.R., Donelan, M.A., 2007. Wave-Follower field measurements of the wind-input spectral function. Part III: parameterization of the wind-input enhancement due to wave breaking. *J. Phys. Oceanogr.* 37 (11), 2764–2775. doi:10.1175/2007JPO3757.1.

Babanin, A.V., Hsu, T.W., Roland, A., Ou, S.H., Doong, D.J., Kao, C.C., 2011. Spectral wave modelling of typhoon Krosa. *Nat. Hazards Earth Syst. Sci.* 11 (2), 501–511. doi:10.5194/nhess-11-501-2011.

Babanin, A.V., Makin, V.K., 2008. Effects of wind trend and gustiness on the sea drag: Lake George study. *J. Geophys. Res.* 113 (C2), C02015. doi:10.1029/2007JCO04233.

Babanin, A.V., Onorato, M., Qiao, F., 2012. Surface waves and wave-coupled effects in lower atmosphere and upper ocean. *J. Geophys. Res.* 117, 1–10. doi:10.1029/2012JC007932.

Babanin, A.V., Tsagareli, K.N., Young, I.R., Walker, D.J., 2010. Numerical investigation of spectral evolution of wind waves. Part II: dissipation term and evolution tests. *J. Phys. Oceanogr.* 40 (4), 667–683. doi:10.1175/2009JPO4370.1.

Bidlot, J.-R., 2012. Present status of wave forecasting at E.C.M.W.F. In: *ECMWF-Workshop on Ocean Waves*, Shinfield Park, Reading, RG2 9AX, United Kingdom, p. 16.

Bidlot, J.-R., Janssen, P., Abdalla, S., 2007. *A Revised Formulation of Ocean Wave Dissipation and Its Model Impact*. Technical Report 509. European Centre for Medium-Range Weather Forecasts, Shinfield Park, Reading, RG2 9AX, England.

Black, P.G., D'Asaro, E.A., Sanford, T.B., Drennon, W.M., Zhang, J.A., French, J.R., Niler, P.P., Terrill, E.J., Walsh, E.J., 2007. AirSea exchange in hurricanes: synthesis of observations from the coupled boundary layer AirSea transfer experiment. *Bull. Am. Meteorol. Soc.* 88 (3), 357–374. doi:10.1175/BAMS-88-3-357.

Booij, N., Ris, R.C., Holthuijsen, L.H., 1999. A third-generation wave model for coastal regions: 1. Model description and validation. *J. Geophys. Res.* 104 (C4), 7649–7666. doi:10.1029/98JC02622.

Cardone, V.J., Cox, A.T., 2009. Tropical cyclone wind field forcing for surge models: critical issues and sensitivities. *Nat. Hazards* 51 (1), 29–47. doi:10.1007/s11069-009-9369-0.

Cardone, V.J., Jensen, R.E., Resio, D.T., Swail, V.R., Cox, A.T., 1996. Evaluation of contemporary ocean wave models in rare extreme events: the "halloween storm" of October 1991 and the "Storm of the Century" of March 1993. *J. Atmos. Oceanic Technol.* 13 (1), 198–230. doi:10.1175/1520-0426(1996)013<0198:EOCOWM>2.0.CO;2.

Cavaleri, L., 2009. Wave modeling – missing the peaks. *J. Phys. Oceanogr.* 39 (11), 2757–2778. doi:10.1175/2009JPO4067.1.

Cavaleri, L., Alves, J.H.G.M., Ardhuin, F., Babanin, A., Banner, M., Belibassakis, K., Benoit, M., Donelan, M., Groeneweg, J., Herbers, T.H.C., Hwang, P., Janssen, P.A.E.M., Janssen, T., Lavrenov, I.V., Magne, R., Monbaliu, J., Onorato, M., Polnikov, V., Resio, D., Rogers, W.E., Sheremet, A., McKee Smith, J., Tolman, H.L., van Vledder, G., Wolf, J., Young, I., 2007. Wave modelling – the state of the art. *Prog. Oceanogr.* 75 (4), 603–674. doi:10.1016/j.pocan.2007.05.005.

Chalikov, D.V., Belevich, M.Y., 1993. One-dimensional theory of the wave boundary layer. *Boundary Layer Meteorol.* 63 (1–2), 65–96. doi:10.1007/BF00705377.

Chao, Y.Y., Tolman, H.L., 2010. Performance of NCEP regional wave models in predicting peak sea states during the 2005 North Atlantic hurricane season*. *Weather Forecasting* 25 (5), 1543–1567. doi:10.1175/2010WAF2222309.1.

Chen, S.S., Curcic, M., 2015. Ocean surface waves in hurricane Ike (2008) and super-storm Sandy (2012): coupled model predictions and observations. *Ocean Modell.* doi:10.1016/j.ocemod.2015.08.005.

Chen, S.S., Price, J.F., Zhao, W., Donelan, M.A., Walsh, E.J., 2007. The CBLAST-hurricane program and the next-generation fully coupled atmosphere-wave-ocean models for hurricane research and prediction. *Bull. Am. Meteorol. Soc.* 88 (3), 311–317. doi:10.1175/BAMS-88-3-311.

Cummings, J.A., 2005. Operational multivariate ocean data assimilation. *Q. J. R. Meteorol. Soc.* 131 (613), 3583–3604.

Cummings, J.A., Smedstad, O.M., 2013. *Variational data assimilation for the global ocean. In: Data Assimilation for Atmospheric, Oceanic and Hydrologic Applications (Vol. II)*. Springer, pp. 303–343.

Dietrich, J.C., Westerink, J.J., Kennedy, A.B., Smith, J.M., Jensen, R.E., Zijlema, M., Holthuijsen, L.H., Dawson, C., Luettich, R.A., Powell, M.D., Cardone, V.J., Cox, A.T., Stone, G.W., Pourtaheri, H., Hope, M.E., Tanaka, S., Westerink, L.G., Westerink, H.J., Cobell, Z., 2011. Hurricane Gustav (2008) waves and storm surge: hindcast, synoptic analysis, and validation in southern Louisiana. *Mon. Weather Rev.* 139 (8), 2488–2522. doi:10.1175/2011MWR3611.1.

Donelan, M., 1999. Wind-induced growth and attenuation of laboratory waves. In: *Institute of Mathematics and Its Applications Conference Series*, 69. Oxford; Clarendon; 1999, pp. 183–194.

Donelan, M.A., Babanin, A.V., Young, I.R., Banner, M.L., 2006. Wave-Follower field measurements of the wind-input spectral function. Part II: parameterization of the wind input. *J. Phys. Oceanogr.* 36 (8), 1672–1689. doi:10.1175/JPO2933.1.

Donelan, M.A., Curcic, M., 2012. The University of Miami Wave Model (UMWM) Version 1.01. University of Miami, Rosenstiel School of Marine and Atmospheric Science.

Donelan, M.A., Curcic, M., Chen, S.S., Magnusson, A.K., 2012. Modeling waves and wind stress. *J. Geophys. Res.* 117 (November 2011), C00J23. doi:10.1029/2011JC007787.

Donelan, M.A., Drennon, W.M., Katsaros, K.B., 1997. The AirSea momentum flux in conditions of wind sea and swell. *J. Phys. Oceanogr.* 27 (10), 2087–2099.

Donelan, M.A., Hamilton, J., Hui, W., 1985. Directional spectra of wind-generated waves. *Philos. Trans. R. Soc. London A* 315 (1534), 509–562.

Donelan, M.A., Haus, B.K., Reul, N., Plant, W.J., Stiassnie, M., Graber, H.C., Brown, O.B., Saltzman, E.S., 2004. On the limiting aerodynamic roughness of the ocean in very strong winds. *Geophys. Res. Lett.* 31 (18), L18306. doi:10.1029/2004GL019460.

Edson, J.B., Jampana, V., Weller, R.A., Bigorre, S.P., Plueddemann, A.J., Fairall, C.W., Miller, S.D., Mahrt, L., Vickers, D., Hersbach, H., 2013. On the exchange of momentum over the open ocean. *J. Phys. Oceanogr.* 43 (8), 1589–1610. doi:10.1175/JPO-D-12-0173.1.

Fan, Y., Ginis, I., Hara, T., 2009. The effect of WindWaveCurrent interaction on AirSea momentum fluxes and ocean response in tropical cyclones. *J. Phys. Oceanogr.* 39 (4), 1019–1034. doi:10.1175/2008JPO4066.1.

- Fan, Y., Ginis, I., Hara, T., Wright, C.W., Walsh, E.J., 2009. Numerical simulations and observations of surface wave fields under an extreme tropical cyclone. *J. Phys. Oceanogr.* 39 (9), 2097–2116. doi:10.1175/2009JPO4224.1.
- Fan, Y., Rogers, W., 2016. Drag coefficient comparisons between observed and model simulated directional wave spectra under hurricane conditions. *Ocean Modell.* 102, 1–13. doi:10.1016/j.ocemod.2016.04.004.
- Hasselmann, K., 1962. On the non-linear energy transfer in a gravity-wave spectrum part I. *General theory. J. Fluid Mech.* 12 (04), 481–500.
- Hasselmann, S., Hasselmann, K., Allender, J.H., Barnett, T.P., 1985. Computations and parameterizations of the nonlinear energy transfer in a gravity-wave spectrum. Part II: parameterizations of the nonlinear energy transfer for application in wave models. *J. Phys. Oceanogr.* 15 (11), 1378–1392. doi:10.1175/1520-0485(1985)015<1378:CAPOTN>2.0.CO;2.
- Holthuijsen, L.H., 2007. *Waves in Oceanic and Coastal Waters*. Cambridge University Press.
- Holthuijsen, L.H., Powell, M.D., Pietrzak, J.D., 2012. Wind and waves in extreme hurricanes. *J. Geophys. Res.* 117 (9), 1–15. doi:10.1029/2012JC007983.
- Hu, K., Chen, Q., 2011. Directional spectra of hurricane-generated waves in the Gulf of Mexico. *Geophys. Res. Lett.* 38 (19), 1–7. doi:10.1029/2011GL049145.
- Hwang, P.A., 2011. A note on the ocean surface roughness spectrum. *J. Atmos. Oceanic Technol.* 28 (3), 436–443. doi:10.1175/2010JTECH0812.1.
- Hwang, P.A., 2016. Fetch- and duration-limited nature of surface wave growth inside tropical cyclones: with applications to air-sea exchange and remote sensing*. *J. Phys. Oceanogr.* 46, 41–56. doi:10.1175/JPO-D-15-0173.1.
- Hwang, P.A., Walsh, E.J., 2016. Azimuthal and radial variation of wind-generated surface waves inside tropical cyclones. *J. Phys. Oceanogr.* 46 (9), 2605–2621. doi:10.1175/JPO-D-16-0051.1.
- Janssen, P., 2004. *The Interaction of Ocean Waves and Wind*. Cambridge University Press.
- Janssen, P.A.E.M., 1991. Quasi-linear theory of wind-wave generation applied to wave forecasting. *J. Phys. Oceanogr.* 21 (11), 1631–1642. doi:10.1175/1520-0485(1991)021<1631:QLTOWW>2.0.CO;2.
- Jaroszc, E., Mitchell, D.A., Wang, D.W., Teague, W.J., 2007. Bottom-up determination of air-sea momentum exchange under a major tropical cyclone. *Science* 315, 1707–1709.
- Kahma, K.K., Donelan, M.A., Drennan, W.M., Terray, E.A., 2016. Evidence of energy and momentum flux from swell to wind. *J. Phys. Oceanogr.* 46 (7), 2143–2156. doi:10.1175/JPO-D-15-0213.1.
- Khandekar, M., Lalbeharry, R., Cardone, V., 1994. The performance of the Canadian spectral ocean wave model (CSOWM) during the grand banks ERS-1 SAR wave spectra validation experiment. *Atmos. Ocean* 32 (1), 31–60.
- Komen, G.J., Cavaleri, L., Donelan, M., Hasselmann, K., Hasselmann, S., Janssen, P., 1994. *Dynamics and Modelling of Ocean Waves*. Cambridge university press.
- Komen, G.J., Hasselmann, K., Hasselmann, K., 1984. On the existence of a fully developed wind-sea spectrum. *J. Phys. Oceanogr.* 14 (8), 1271–1285. doi:10.1175/1520-0485(1984)014<1271:OTEOAF>2.0.CO;2.
- Leckler, F., Ardhuin, F., Filippot, J.F., Mironov, A., 2013. Dissipation source terms and whitecap statistics. *Ocean Modell.* 70, 62–74. doi:10.1016/j.ocemod.2013.03.007.
- Liu, Q., Babanin, A.V., Guan, C., Zieger, S., Sun, J., Jia, Y., 2016. Calibration and validation of HY-2 altimeter wave height. *J. Atmos. Oceanic Technol.* 33 (5), 919–936. doi:10.1175/JTECH-D-15-0219.1.
- Liu, Q., Babanin, A.V., Zieger, S., Young, I.R., Guan, C., 2016. Wind and wave climate in the Arctic ocean as observed by altimeters. *J. Clim.* 29 (22), 7957–7975. doi:10.1175/JCLI-D-16-0219.1.
- Mitsuyasu, H., Tasai, F., Suhara, T., Mizuno, S., Ohkusu, M., Honda, T., Rikiishi, K., 1975. Observations of the directional spectrum of ocean waves using a Cloverleaf Buoy. *J. Phys. Oceanogr.* 5 (4), 750–760.
- Montoya, R., Arias, A.O., Royero, J.O., Ocampo-Torres, F., 2013. A wave parameters and directional spectrum analysis for extreme winds. *Ocean Eng.* 67, 100–118.
- Moon, I.-J., Ginis, I., Hara, T., 2003. Numerical simulation of sea surface directional wave spectra under typhoon wind forcing. *J. Phys. Oceanogr.* 33 (8), 1680–1706. doi:10.1016/S1001-6058(09)60015-9.
- Moon, I.-J., Ginis, I., Hara, T., 2004. Effect of surface waves on AirSea momentum exchange. Part II: behavior of drag coefficient under tropical cyclones. *J. Atmos. Sci.* 61 (19), 2334–2348. doi:10.1175/1520-0469(2004)061<2334:EOSWOA>2.0.CO;2.
- Moon, I.-J., Ginis, I., Hara, T., 2008. Impact of the reduced drag coefficient on ocean wave modeling under hurricane conditions. *Mon. Weather Rev.* 136 (3), 1217–1223. doi:10.1175/2007MWR2131.1.
- Moon, I.-J., Ginis, I., Hara, T., Thomas, B., 2007. A physics-based parameterization of AirSea momentum flux at high wind speeds and its impact on hurricane intensity predictions. *Mon. Weather Rev.* 135 (8), 2869–2878. doi:10.1175/MWR3432.1.
- Perrie, W., Toulany, B., Resio, D.T., Roland, A., Auclair, J.P., 2013. A two-scale approximation for wave-wave interactions in an operational wave model. *Ocean Modell.* 70, 38–51. doi:10.1016/j.ocemod.2013.06.008.
- Powell, M.D., Houston, S.H., 1996. Hurricane Andrew's landfall in South Florida. Part II: surface wind fields and potential real-time applications. *Weather Forecasting* 11 (3), 329–349. doi:10.1175/1520-0434(1996)011<0329:HALISF>2.0.CO;2.
- Powell, M.D., Houston, S.H., Amat, L.R., Morisseau-Leroy, N., 1998. The HRD real-time hurricane wind analysis system. *J. Wind Eng. Ind. Aerodyn.* 77–78, 53–64. doi:10.1016/S0167-6105(98)00131-7.
- Powell, M.D., Houston, S.H., Reinhold, T.A., 1996. Hurricane Andrew's landfall in South Florida. Part I: standardizing measurements for documentation of surface wind fields. *Weather Forecasting* 11 (3), 304–328. doi:10.1175/1520-0434(1996)011<0304:HALISF>2.0.CO;2.
- Powell, M.D., Murillo, S., Dodge, P., Uhlhorn, E., Gamache, J., Cardone, V., Cox, A., Otero, S., Carrasco, N., Annane, B., Fleur, R.S., 2010. Reconstruction of hurricane Katrina's wind fields for storm surge and wave hindcasting. *Ocean Eng.* 37 (1), 26–36. doi:10.1016/j.oceaneng.2009.08.014.
- Powell, M.D., Vickery, P.J., Reinhold, T.A., 2003. Reduced drag coefficient for high wind speeds in tropical cyclones. *Nature* 422 (6929), 279–283. doi:10.1038/nature01481.
- Rascle, N., Ardhuin, F., 2013. A global wave parameter database for geophysical applications. Part 2: model validation with improved source term parameterization. *Ocean Modell.* 70, 174–188. doi:10.1016/j.ocemod.2012.12.001.
- Reichl, B.G., Hara, T., Ginis, I., 2014. Sea state dependence of the wind stress over the ocean under hurricane winds. *J. Geophys. Res.* 119 (November 2013), 30–51. doi:10.1002/2013JC009289.
- Resio, D.T., Perrie, W., 1991. A numerical study of nonlinear energy fluxes due to wave-wave interactions. Part 1: methodology and basic results. *J. Fluid Mech.* 223, 603–629.
- Resio, D.T., Perrie, W., 2008. A two-scale approximation for efficient representation of nonlinear energy transfers in a wind wave spectrum. Part i: theoretical development. *J. Phys. Oceanogr.* 38 (12), 2801–2816.
- Rogers, E.W., Babanin, A.V., Wang, D.W., 2012. Observation-consistent input and whitecapping dissipation in a model for wind-generated surface waves: description and simple calculations. *J. Atmos. Oceanic Technol.* 29 (9), 1329–1346. doi:10.1175/JTECH-D-11-00092.1.
- Rogers, W.E., Van Vledder, G.P., 2013. Frequency width in predictions of windsea spectra and the role of the nonlinear solver. *Ocean Modell.* 70, 52–61. doi:10.1016/j.ocemod.2012.11.010.
- Roland, A., 2008. *Development of WWM II: Spectral Wave Modelling on Unstructured Meshes*. Ph.D. thesis Technische Universität Darmstadt, Institute of Hydraulic and Water Resources Engineering.
- Sitkowski, M., Kossin, J.P., Rozoff, C.M., 2011. Intensity and structure changes during hurricane eyewall replacement cycles. *Mon. Weather Rev.* 139, 3829–3847. doi:10.1175/MWR-D-11-00034.1.
- Smith, T.A., Chen, S., Campbell, T., Martin, P., Rogers, W.E., Gaberšek, S., Wang, D., Carroll, S., Allard, R., 2013. Ocean-wave coupled modeling in COAMPS-TC: a study of hurricane Ivan (2004). *Ocean Modell.* 69, 181–194. doi:10.1016/j.ocemod.2013.06.003.
- Soloviev, A.V., Lukas, R., Donelan, M.A., Haus, B.K., Ginis, I., 2014. The air-sea interface and surface stress under tropical cyclones. *Sci. Rep.* 4, 5306. doi:10.1038/srep05306.
- Stopa, J.E., Ardhuin, F., Babanin, A., Zieger, S., 2016. Comparison and validation of physical wave parameterizations in spectral wave models. *Ocean Modell.* 103, 2–17.
- Takagaki, N., Komori, S., Suzuki, N., Iwano, K., Kuramoto, T., Shimada, S., Kurose, R., Takahashi, K., 2012. Strong correlation between the drag coefficient and the shape of the wind sea spectrum over a broad range of wind speeds. *Geophys. Res. Lett.* 39 (23), 1–6. doi:10.1029/2012GL053988.
- Taylor, K.E., 2001. Summarizing multiple aspects of model performance in a single diagram. *J. Geophys. Res.* 106 (D7), 7183–7192.
- Terwey, W.D., Montgomery, M.T., 2008. Secondary eyewall formation in two idealized, full-physics modeled hurricanes. *J. Geophys. Res. Atmos.* 113 (12), 1–18. doi:10.1029/2007JD008897.
- The WAMDI Group, 1988. The WAM model - a third generation ocean wave prediction model. *J. Phys. Oceanogr.* 18 (12), 1775–1810. doi:10.1175/1520-0485(1988)018<1775:TWMTGO>2.0.CO;2.
- Tolman, H., 2002. *Validation of WAVEWATCH III Version 1.15 for a Global Domain*. Technical Report 213. Environmental Modeling Center, Ocean Modeling Branch.
- Tolman, H.L., 1991. A third-generation model for wind waves on slowly varying, unsteady, and inhomogeneous depths and currents. *J. Phys. Oceanogr.* 21 (6), 782–797. doi:10.1175/1520-0485(1991)021<0782:ATGMFW>2.0.CO;2.
- Tolman, H.L., 2010. *Optimum Discrete Interaction Approximations for Wind Waves. Part 4: Parameter Optimization*. Technical Report 288. Environmental Modeling Center, Marine Modeling and Analysis Branch.
- Tolman, H.L., 2013. A generalized multiple discrete interaction approximation for resonant four-wave interactions in wind wave models. *Ocean Modell.* 70, 11–24. doi:10.1016/j.ocemod.2013.02.005.
- Tolman, H.L., Alves, J.-H.G., 2005. Numerical modeling of wind waves generated by tropical cyclones using moving grids. *Ocean Modell.* 9 (4), 305–323. doi:10.1016/j.ocemod.2004.09.003.
- Tolman, H.L., Alves, J.-H.G.M., Chao, Y.Y., 2005. Operational forecasting of wind-generated waves by hurricane Isabel at NCEP*. *Weather Forecasting* 20 (4), 544–557. doi:10.1175/WAF852.1.
- Tolman, H.L., Banner, M.L., Kaihatu, J.M., 2013. The NOPP operational wave model improvement project. *Ocean Modell.* 70, 2–10. doi:10.1016/j.ocemod.2012.11.011.
- Tolman, H.L., Chalikov, D., 1996. *Source terms in a third-generation wind wave model. J. Phys. Oceanogr.* 26, 2497–2518.
- Tolman, H.L., Grumbine, R.W., 2013. Holistic genetic optimization of a generalized multiple discrete interaction approximation for wind waves. *Ocean Modell.* 70, 25–37. doi:10.1016/j.ocemod.2012.12.008.
- Tolman, H. L., The WAVEWATCH III Development Group, 2014. *User Manual and System Documentation of WAVEWATCH III Version 4.18*. Environmental Modeling Center, Marine Modeling and Analysis Branch, National Centers for Environmental Prediction.
- Tracy, B., Resio, D.T., 1982. *Theory and Calculation of the Nonlinear Energy Transfer Between Sea Waves in Deep Water*. WES Report 11. US Army Corps of Engineers.

- Tsagareli, K.N., Babanin, A.V., Walker, D.J., Young, I.R., 2010. Numerical investigation of spectral evolution of wind waves. Part I: wind-input source function. *J. Phys. Oceanogr.* 40 (4), 656–666. doi:[10.1175/2009JPO4345.1](https://doi.org/10.1175/2009JPO4345.1).
- van Vledder, G.P., 2006. The WRT method for the computation of non-linear four-wave interactions in discrete spectral wave models. *Coastal Eng.* 53 (2–3), 223–242. doi:[10.1016/j.coastaleng.2005.10.011](https://doi.org/10.1016/j.coastaleng.2005.10.011).
- Wang, D.W., Mitchell, D.A., Teague, W.J., Jarosz, E., Hulbert, M.S., 2005. Extreme waves under hurricane Ivan. *Science* 309 (5736). doi:[10.1126/science.1112509](https://doi.org/10.1126/science.1112509). 896–896
- Warner, J.C., Armstrong, B., He, R., Zambon, J.B., 2010. Development of a coupled ocean-atmosphere-wave-sediment transport (COAWST) modeling system. *Ocean Modell.* 35 (3), 230–244. doi:[10.1016/j.ocemod.2010.07.010](https://doi.org/10.1016/j.ocemod.2010.07.010).
- Webb, D.J., 1978. Non-linear transfers between sea waves. *Deep-Sea Res.* 25, 279–298.
- Wright, C.W., Walsh, E.J., Vandemark, D., Krabill, W.B., Garcia, A.W., Houston, S.H., Powell, M.D., Black, P.G., Marks, F.D., 2001. Hurricane directional wave spectrum spatial variation in the open ocean. *J. Phys. Oceanogr.* 31, 2472–2489.
- Wu, J., 1982. Wind-stress coefficients over sea surface from breeze to hurricane. *J. Geophys. Res.* 87, 9704–9706.
- Young, I.R., 1999. *Wind Generated Ocean Waves*. Elsevier Science Ltd.
- Young, I.R., 2003. A review of the sea state generated by hurricanes. *Mar. Struct.* 16 (3), 201–218. doi:[10.1016/S0951-8339\(02\)00054-0](https://doi.org/10.1016/S0951-8339(02)00054-0).
- Young, I.R., 2006. Directional spectra of hurricane wind waves. *J. Geophys. Res.* 111 (8), 1–14. doi:[10.1029/2006JC003540](https://doi.org/10.1029/2006JC003540).
- Young, I.R., Babanin, A.V., 2006. Spectral distribution of energy dissipation of wind-generated waves due to dominant wave breaking. *J. Phys. Oceanogr.* 36 (3), 376–394.
- Young, I.R., Zieger, S., Babanin, A.V., 2011. Global trends in wind speed and wave height. *Science* 332, 451–455. doi:[10.1126/science.1197219](https://doi.org/10.1126/science.1197219).
- Zieger, S., Babanin, A.V., Rogers, W.E., Young, I.R., 2015. Observation-based source terms in the third-generation wave model WAVEWATCH. *Ocean Modell.* 218, 1–24. doi:[10.1016/j.ocemod.2015.07.014](https://doi.org/10.1016/j.ocemod.2015.07.014).
- Zieger, S., Vinoth, J., Young, I.R., 2009. Joint calibration of multiplatform altimeter measurements of wind speed and wave height over the past 20 years. *J. Atmos. Oceanic Technol.* 26, 2549–2564. doi:[10.1175/2009JTECHA1303.1](https://doi.org/10.1175/2009JTECHA1303.1).
- Zijlema, M., Van Vledder, G.P., Holthuijsen, L.H., 2012. Bottom friction and wind drag for wave models. *Coastal Eng.* 65, 19–26. doi:[10.1016/j.coastaleng.2012.03.002](https://doi.org/10.1016/j.coastaleng.2012.03.002).